Evolution of Great Salt Lake's Exposed Lakebed (1984-2023): Variations in Sediment Composition, Water, and Vegetation from Landsat OLI and Sentinel MSI Satellite Reflectance Data

Mark H. Radwin and Brenda B. Bowen
University of Utah, Salt Lake City, Utah, markradwin@gmail.com

10.31711/ugap.v51i.134

ABSTRACT

The Great Salt Lake has been rapidly shrinking since the highstand of the mid-1980s, creating cause for concern in recent decades as the lake has reached historic lows. Many investigators have assessed the evolution of lake elevation, geochemistry, anthropogenic impacts, and links to climate and atmospheric processes; however, the use of remote sensing to study the evolution of the lake has been significantly limited. Harnessing recent advancements in cloud-processing, specifically Google Earth Engine cloud computing, this study utilizes over 600 Landsat TM/OLI and Sentinel MSI satellite images from 1984-2023 to present time-series analyses of remotely sensed Great Salt Lake water area, exposed lakebed area, surface cover types, and chlorophyll-a analyses paired with modelled estimates for water and exposed lakebed area. Results show that since the highstand of 1986-1987, the water area has declined by 45% (~3,000 km^2) and the exposed lakebed area has increased to ~3,500 km^2 from ~500 km^2. The area of unconsolidated sediments not protected by vegetation or halite crusts has risen to ~2,400 km^2. Significant halite crusts are observed in the North Arm, having a max extent of ~150 km^2 between 2002 and 2003, while only small extents of halite crusts are observed for the South Arm. Vegetation is more prevalent in the Bear River Bay and South Arm, with surface area increases over 400% since 1990. Gypsum is widely observed independent of halite crusts. The results highlight multiple instances of land-use/water-management that led to observable changes in water/exposed lakebed area and halite crust extent. This study demonstrates the important benefits of maintaining a lake elevation above ~4,194 ft to maximize lake and halite crust area, which would help mitigate possible dust events and maintain a broad lake extent.

INTRODUCTION

In recent years the Great Salt Lake in northern Utah has attracted the attention of local legislators and a global audience as the lake reached historic lows and caused concerns for public health and the health of the overall Great Salt Lake ecosystem. Once part of the vast Pleistocene Lake Bonneville, the Great Salt Lake has shrunk to the modern state from an evaporative evolution in a closed basin with natural inputs from three major rivers (Bear, Jordan, and Weber rivers). However, in recent centuries, anthropogenic activity has considerably affected the Great Salt Lake. This influence extends to direct physical alterations of the lake's landscape, modifications to its hydrology that alter water flow and distribution, the introduction of invasive plant species, and extensive resource extraction. In 1959 a railroad causeway was completed, separating the lake into a North and South Arm, which has been modified over the years with various breaches, culverts, and berms to control flow between the flow between the two arms (Figure 1). Additionally, the railroad causeway, mineral operator evaporation ponds, and other various impoundments have significantly separated and controlled the flow from Bear River Bay to the South Arm. With the North Arm largely cut-off from major river inputs, it has evolved to be much more saline and commonly surpasses halite saturation, leading to precipitation of lake-bottom and shoreline halite crusts as well as a different color of water due to halophilic microorganisms. The lake has been used by wildlife as a crucial bird migratory location and anthropogenically for resource extraction. In the 1980s the lake rose nearly 8 ft due to an unusually heavy period of precipitation between 1982 and 1987, but has been steadily shrinking since, reaching a historic low in 2022. With the ongoing reduction in the lake's size, there is an escalating risk of moderate-to-severe dust storms associated with lakebed exposure and substantial changes in the ecosystem, which could adversely impact bird migrations. Additionally, the overall stability of the regional ecosystem is becoming increasingly compromised.

Many aspects of the Great Salt Lake's evolution are well documented. Since the mid-1800s the US Geological Survey has been recording lake elevations and water quality metrics, and since the mid-1900s

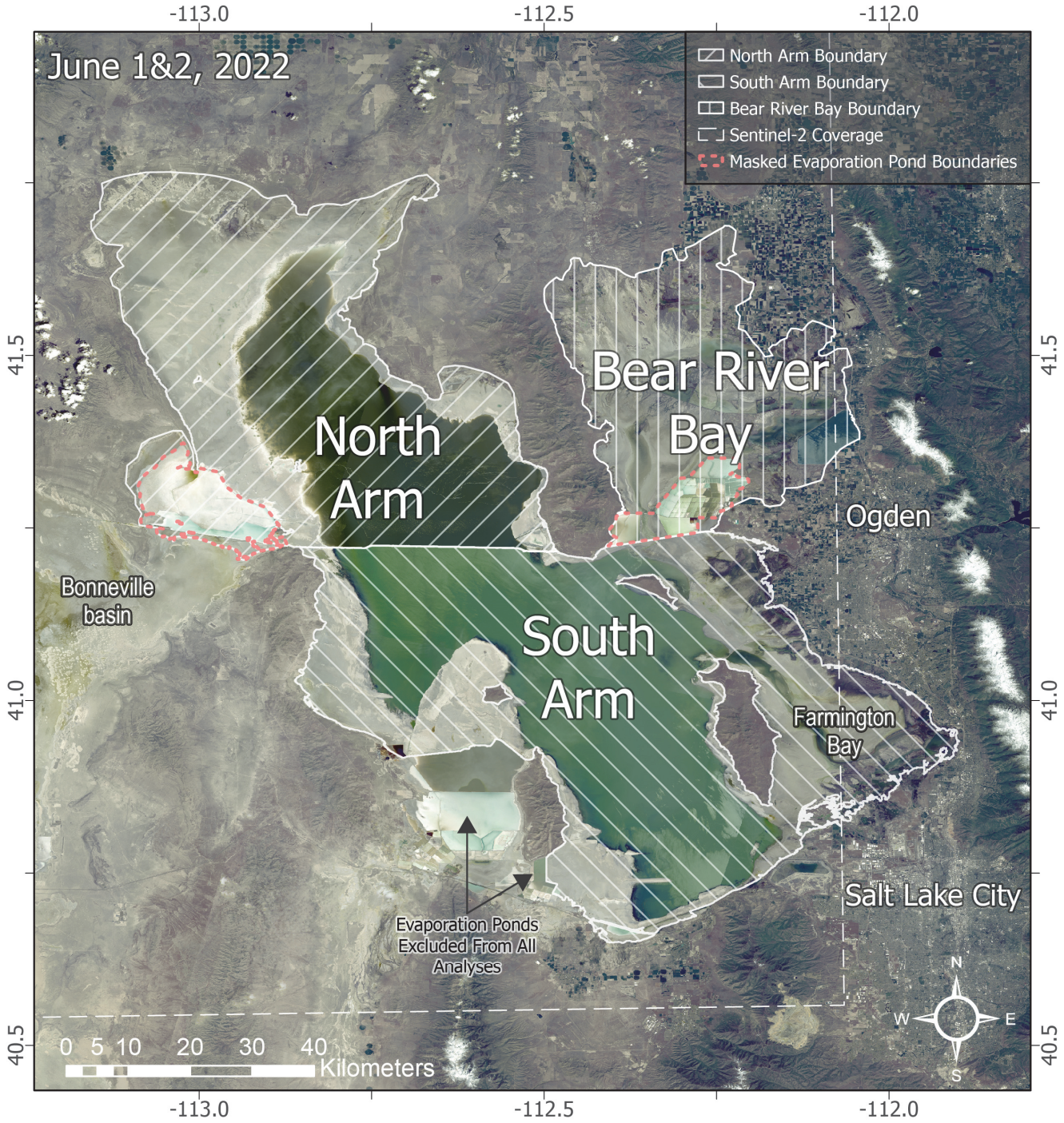

Figure 1. *Map of the Great Salt Lake system and surrounding localities, including boundaries for the North Arm, South Arm, and Bear River Bay. Also defined are the boundaries of the North Arm mineral operator evaporation pools included in analyses between 1984-1994 and the evaporation pool masked for halite analyses in the Bear River Bay. The dashed rectangular line indicates the area captured by the Sentinel-2 MSI satellite and the base-map is Landsat 8 OLI imagery from June 1st (south image) and 2nd (north image).*

the Utah Geological Survey has been recording geochemical measurements (Arnow, 1984; Gwynn, 2007; Rupke and McDonald, 2012; Naftz and others, 2013). In recent decades investigators have started assessing the contributing factors to the decline of the Great Salt Lake through water balance models, finding anthropogenic reduction of inflow and drought conditions (precipitation/inflow) to be the leading drivers of lake decline, with climate (evaporation) being a secondary factor (Mohammed and Tarboton, 2012; Wurtsbaugh and others, 2016; Wurtsbaugh and others, 2017; Wine and others, 2019; Null and Wurtsbaugh, 2020; Wurtsbaugh and Sima, 2022). More recent reports have constrained the impact of natural and human consumptive use to be responsible for 67-73% of the Great Salt Lake water loss

(Ahmadi and others, 2023). Other studies have observed relationships between atmospheric oscillations in the Pacific and multidecadal drought conditions which directly affect Great Salt Lake levels, and determined that although climate change will lower lake levels through higher temperatures, evaporation, and changes in the snowmelt cycle, those impacts will be overshadowed by anthropogenic water withdrawal and drought conditions (Wang and others, 2012; Mohammed and Tarboton, 2012; Wine and others, 2019; Hall and others, 2021; Ahmadi and others, 2023). Further, climate models suggest there will be an increase in precipitation with a warmer climate, but increases in precipitation will be negated by a greater increase in evaporation (Ahmadi and others, 2023).

Related to the impacts of a shrinking Great Salt Lake, others have investigated dust sources around the shoreline, impacts from dust events and dust-on-snow, pollutant contamination of dust-derived-sediments, regional land cover changes, and the atmospheric characteristics of dust events, all finding Great Salt Lake sediments to be a significant dust source in northern Utah (Hahnenberger and Nicoll, 2012; Hahnenberger and Nicoll, 2014; Skiles and others, 2018; Perry and others, 2019; Nicoll and others, 2020; Carling and others, 2020). Although these aspects of the lake are well documented, the use of remote sensing to document the changing Great Salt Lake system is only limited to water-surface-temperature, algal blooms, outdated classification maps, and the common use of side-by-side true-color satellite image comparisons (Hung and Wu, 2005; Bradt and others, 2006; Crosman and Horel, 2009; Hansen and others, 2016).

Here, multispectral remote sensing data of the Great Salt Lake from 1984 to 2023 are used to assess the evolution of sediment types and sediment area, vegetation area, water area, and relative chlorophyll-a concentrations between the North Arm, South Arm (including the Farmington Bay), and Bear River Bay. The NASA/USGS Landsat 5 Thematic Mapper (TM), Landsat 8 Operational Land Imager (OLI), and Landsat 9 OLI, as well as the ESA Sentinel 2 A&B Multi-Spectral Instrument (MSI) satellite platforms are chosen for this study, where the Landsat imagery extends back to the 1980's while the Sentinel imagery extends back to 2019 for this region. Combining these datasets results in over 600 near-cloud-free satellite scenes of the region from 1984 to 2023. Historically, this volume of data prevented analyses due to the sheer amount of work and processing power involved, but has recently become feasible through automation and cloud-processing platforms. The results will help to understand the evolution of exposed sediments, halite crust formation, changes in vegetation, and the relationships between land-use, climate, and increasing sediment area. This work builds off of recent remote sensing studies in the Bonneville basin which utilized Landsat 5 TM and 8 OLI multispectral imagery to map halite, gypsum, and carbonate-muds (lacustrine detritus; Bowen et al., 2017; Radwin & Bowen, 2021).

METHODS

Data Sources and Cloud Processing

The Landsat TM/OLI and Sentinel MSI platforms were used for this analysis as these sensors can capture the entire extent of either arm of the Great Salt Lake and Bear River Bay during a single swath path, have suitable spatial and spectral band wavelengths for investigating surface features and types, theoretically allow for at least one image acquisition per month, and have longevity with multispectral data extending back to the 1980s. The Landsat 5 TM, 8 OLI, and 9 OLI platforms have a spatial resolution of 30 m/pixel and seven bands (six for TM) ranging the VSWIR spectrum (~350-2500 nm), with a revisit time of 16 days (Table 1). The Landsat 5 platform was operational from 1984 to 2012, and the Landsat 8 and 9 platforms have been operational since 2013 and 2021, respectively. The Sentinel-2 MSI platform, operational since 2015, has a spatial resolution that ranges from 10-60 m/pixel (max 20 m/pixel used in this study) and 12 bands ranging the VSWIR spectrum (Table 1), with a revisit time of 10 days (5-days including both A&B satellites).

Although the Sentinel-2 platform has been active since 2015, images for Utah were not acquired until very late 2018. Additionally, the extent of the Sentinel swath fails to image the entirety of the Farmington Bay region (Figure 1 - dashed white line), but this is accounted for when comparing to Landsat observations by cropping the Landsat observations for vegetation to the extent of Sentinel 2 tiles. Image acquisition and processing is done in the cloud with Google Earth Engine (GEE), implemented via the GEE Python 3 API in conjunction with the geemap python package for interactive mapping and data export (Amani and others, 2020; Tamiminia and others, 2020; Wu, 2020). Pre-processed, atmospherically corrected Landsat Level 2 (Tier 1, Collection 2) and Sentinel-2 Level-2A (harmonized) reflectance image collections are defined from the base GEE collections, which are then filtered to near-cloud-free images covering the Great Salt Lake region. Landsat 5 TM bands are renamed to match Landsat 8 & 9 OLI specifications, and all the Landsat images are merged into the

Table 1. *Spectral band specifications for Landsat TM, OLI, and Sentinel MSI multispectral sensors.*

Landsat 5 TM				Landsat 8 & 9 OLI				Sentinel 2 MSI			
Band Number	**Band Name**	**Spectral Range (nm)**	**Resolution (m)**	**Band Number**	**Band Name**	**Spectral Range (nm)**	**Resolution (m)**	**Band Number**	**Band Name**	**Spectral Range (nm)**	**Resolution (m)**
1	Blue	450-520	30	1	Coastal Aerosol	433–453	30	1	Coastal Aerosol	433-453	60
2	Green	520-600	30	2	Blue	450–515	30	2	Blue	458-523	10
3	Red	630-690	30	3	Green	525–600	30	3	Green	543-578	10
4	NIR	760-900	30	4	Red	630–680	30	4	Red	650-680	10
5	SWIR 1	1550-1750	30	5	NIR	845–885	30	5	Vegetation Red Edge	698-713	20
6	TIRS	10400-12500	120 (30)	6	SWIR 1	1560–1660	30	6	Vegetation Red Edge	733-748	20
7	SWIR 2	2080-2350	30	7	SWIR 2	2100–2300	30	7	Vegetation Red Edge	773-793	20
				8	Panchro-matic	500–680	15	8	NIR	785-900	10
				9	Cirrus	1360–1390	30	8a	Narrow NIR	855-875	20
				10	TIRS 1	10600-11200	100	9	Water Vapor	935-955	60
				11	TIRS 2	11500-12500	100	10	SWIR – Cirrus	1360-1390	60
								11	SWIR	1565-1655	20
								12	SWIR	2100-2280	20

same collection. Cloudy image filtering is accomplished using image cloud percentage metadata provided by the USGS and ESA (Drusch and others, 2012; Foga and others, 2017; Tiede and others, 2021), where images with less than 10% of the scene covered by clouds are chosen to process for both Landsat and Sentinel imagery. For Sentinel-2, many images were found to have a significant percentage of bad-pixels (no data), thus a bad-pixel filter was applied to remove those images.

The size and swath path of Landsat imagery results in only one complete arm of the lake being imaged for each swath, meaning each arm of the lake is observed on different dates. However, Sentinel-2 can image both arms on the same date. For this reason, all imagery results are split between North and South Arm. The Landsat tile specifications are rows 31 and 32, and paths 38 and 39, while the Sentinel tile specifications are 12TUM and 12TUL. Images with the same date are combined to a single image, but images without a paired same-date southern or northern swath image are discarded as that indicates the other scene isn't suitable and the entire area couldn't be observed. Landsat 1 true-color images from 1972, 1974, and 1979 are used for manual delineation of lake extent to provide a reference prior to the wet 1980's. Landsat 5 images from 1984 are used for manually delineating the extent of the entire Great Salt Lake system, also referencing recent imagery, to be used for masking the data to a boundary and for exposed lakebed area calculations (Figure 1). The exposed lakebed is here defined as the area extending from the shoreline to the imposed Great Salt Lake system boundary (Figure 1) that encompasses lacustrine derived sediments, evaporites, and vegetation.

Select mineral operator evaporation ponds within the project-defined boundary of the Great Salt Lake system are not included in the analyses. These areas include the evaporation ponds to the southwest, west and south of Stansbury Island, and to northeast in the Bear River Bay, which were established prior to 1984, in addition to evaporation ponds to the north-

west. However, the area of the evaporation pond to the northwest, in the North Arm, is included in analyses up until the evaporation pond was constructed in 1994. Similarly, the evaporation ponds situated in the southern region of Bear River Bay are employed for satellite monitoring, with the exception of halite detections. This is to circumvent any false readings caused by halite linked with mining activities. Other evaporation ponds that exist within the study area are not masked-out and are included in analyses, albeit the remaining ponds are small in comparison to the evaporation ponds removed from analyses. The size of the North Arm evaporation pond accounts for ~7.6% of the area within the North Arm boundary (Figure 1).

Spectral Indices

The general mineralogy of the Great Salt Lake exposed lakebed sediments are similar to the sediments in the proximal Bonneville basin (A.K.A., Great Salt Lake Desert) as both landscapes share a provenance (Lake Bonneville) and are connected by a spillway. The general mineralogical suite can be simplified to carbonate-rich lacustrine sediments, that comprise the majority of the sediments, which are overlain or interfingered with gypsum ($CaSO_4 \cdot 2H_2O$) and halite (NaCl) evaporite deposits that vary spatiotemporally. The carbonate-rich lacustrine sediments are subsequently referred to as carbonate-muds, as they are typically an intimate mixture of carbonates (including authigenic coatings/cements/nodules, oolitic sands, skeletal fragments, and intraclasts of calcite or aragonite; $CaCO_3$), quartz grains (SiO_2), and phyllosilicates (clays/muds), but also may contain magnesite ($MgCO_3$), mirabilite ($Na_2SO_4 \cdot 10H_2O$), and other lesser-occurring but still prevalent minerals (Lines, 1979; Pace and others, 2016; Newell and others, 2017; Perry and others, 2019; Dunham and others, 2020; Ingalls and others, 2020; Smith and others, 2020; Jagniecki and others, 2021; Homewood and others, 2022). The grain size distribution as well as proportion of mineralogical components varies spatially for exposed carbonate-muds, but only the surface mineralogy type is considered here (Perry and others, 2019). Gypsum deposits are found precipitating from springs found within the Great Salt Lake system, but much of the gypsum within the system is likely redistributed rather than actively precipitating, as the Great Salt Lake chemistry is calcium limited and now an $MgSO_4$ system (Hardie and Eugster, 1970; Jagniecki and others, 2021). To map these three sediment type classes, each satellite image is processed to mask out other landcover, leaving only surficial sediments, and then each sediment type is differentiated using multispectral indices adapted from work in the Bonneville basin mapping similar surface types (Radwin and Bowen, 2021). To map the extent of water and vegetation, which is used to isolate surficial sediments, the Normalized Difference Water Index (NDWI) and Normalized Difference Vegetation Index (NDVI) are utilized (McFeeters, 1996; Gandhi and others, 2015; Huang and others, 2021). For this study, the halite index takes the form of RED – SWIR1 / RED + SWIR1 and the index for gypsum and carbonate-muds takes the form of SWIR1 – SWIR2 / SWIR1 + SWIR2. The halite index exploits a significant drop in reflectance from the RED (~650 nm) to the SWIR1 (~1600 nm) bands observed in local halite spectra, which is not observed for the other sediment types (Radwin and Bowen, 2021). Likewise, the gypsum index exploits a slight decrease in reflectance between the SWIR1 (~1600 nm) and SWIR2 (~2200 nm) bands observed for local gypsum spectra, which is not typically observed for the local intimate-mixture of carbonates, quartz, or phyllosilicates (carbonate-muds).

All resulting images from surface type indices are masked to the surface type of interest using image histogram thresholds. For Landsat NDWI results, the threshold is sensitive to sensor-type as well as radiometric differences between scenes, and is determined for each image using an adapted Otsu image segmentation technique, which is then offset by +0.15, +0.175, and +0.175 for the North Arm, South Arm, and Bear River Bay, respectively (Otsu, 1979; Ji and others, 2009). The dynamic thresholding is noted to drastically help the accuracy of water detection for Landsat imagery, particularly at the water-shore interface. Other index results use a static threshold for all images, with differing values for Landsat and Sentinel to account for differences between sensors. All static thresholds are determined through incrementally assessing how thresholds perform delineation of surface type boundaries, with the goal of having the threshold provide the greatest separation from background values without including background values in the results. For Landsat indices, the thresholds chosen are: ≥ 0.345 for halite, ≥ 0.153 for gypsum, < 0.153 for carbonate-muds, and ≥ 0.105 for NDVI. For Sentinel, the thresholds chosen are: ≥ 0.58 for halite, ≥ 0.3 for gypsum, < 0.3 for carbonate-muds, ≥ 0.185 for NDVI, and ≥ 0.06 for NDWI. Rather than employ a separate index to map carbonate muds, the gypsum index is also used where all unmasked sediments below the threshold used for gypsum are classified as carbonate-muds or other by process-of-elimination. Dynamic thresholding for Sentinel NDWI images is not applied as there are data-issues associated with bad/no-data pixels that hinder the dynamic threshold

processing for dozens of images with no apparent fix. However, the NDWI threshold for Sentinel appears to be less sensitive compared to Landsat results. For Sentinel-2 MSI gypsum, carbonates, and chlorophyll-a indices, the 10 m/pixel input bands are resampled to 20 m/pixel to match the resolution of the SWIR bands.

To assess relative chlorophyll-a concentrations, the KIVU and 2BDA indices are used for Landsat and Sentinel imagery, respectively (Gitelson and others, 2003; Buma and Lee, 2020). Different indices are chosen as the Sentinel MSI sensor is better suited for chlorophyll detection having red-edge bands. The KIVU index takes the form of BLUE – RED / GREEN while 2BDA takes the form of RED-EDGE-1 / RED.

Processing Workflow

All images are masked to the correct arm of the lake system prior to processing spectral indices. A systematic workflow is implemented to process each surface type index, where the order of processing follows: 1) water (NDWI), 2) vegetation (NDVI), 3) halite, 4) gypsum, and 5) carbonate-muds/other (Figure 2). It is important to note that the results of each index are used to mask the image of the following index, to ensure no pixels are classified twice. For example, the input image for the halite index is masked to be absent of water (NDWI) or vegetation (NDVI) pixels and is theoretically just surficial sediments. The order of processing is chosen as NDWI and NDVI are more standard and broadly applicable spectral techniques that can be used regardless of the surrounding geolog-

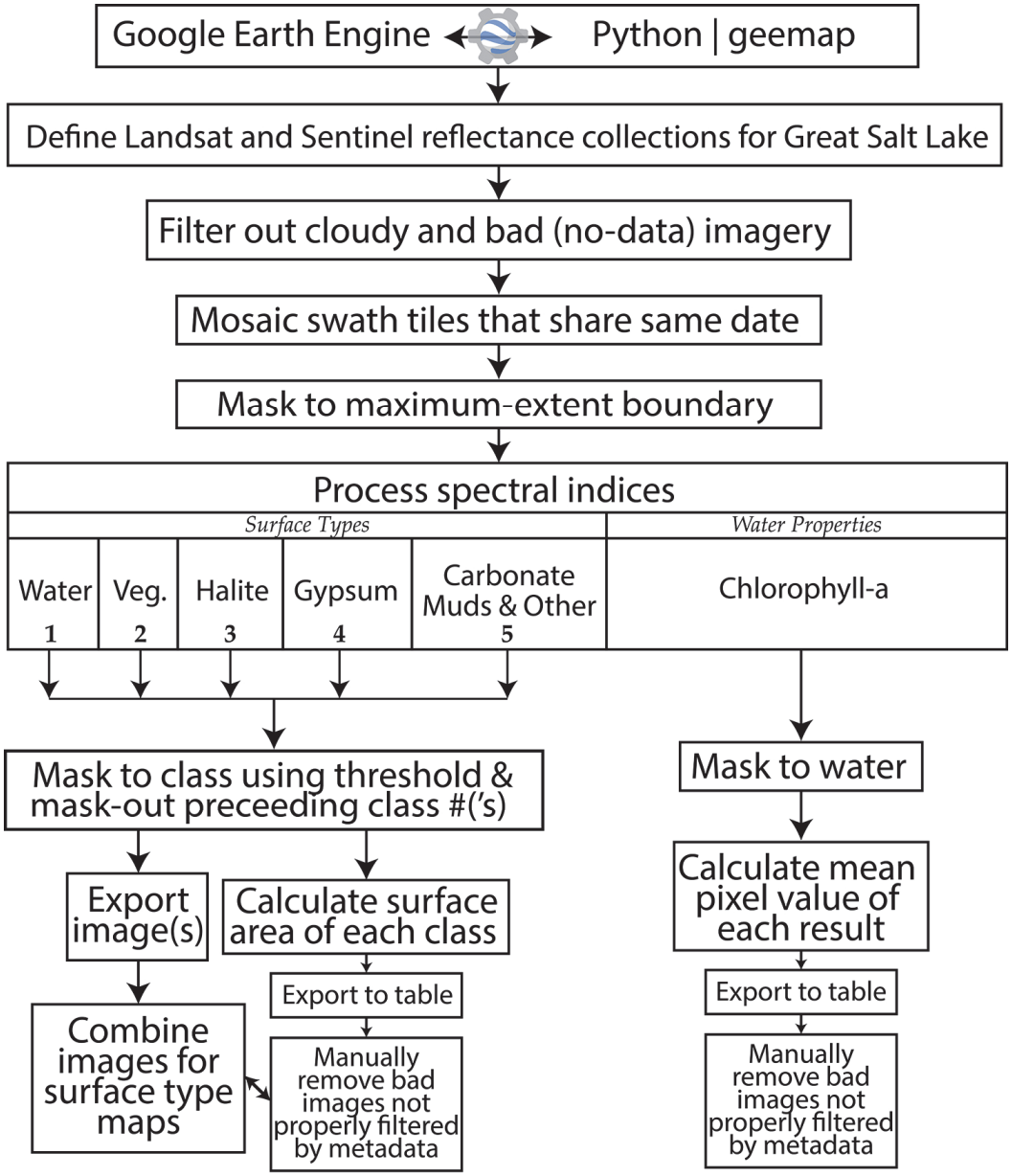

Figure 2. *Workflow chart of methods used to define and process satellite imagery using Google Earth Engine Python API.*

ical/mineralogical context, while the sediment indices rely on the isolation of surficial sediments with the mineralogical framework found in the Great Salt Lake and Lake Bonneville system for the intended performance. The halite index is processed as the first sediment index as it exploits a significant spectral characteristic not found in the other sediments and is believed to be the most sensitive of the mineralogical indices used here. Thus, the order of index calculation and image masking follows the most broad-to-limited applicability for the chosen spectral indices and mitigates water or vegetation false-positives for mineralogical differentiations. Changing the order of NDWI and NDVI should not have much impact, but the order of the sediment indices matters as the gypsum index can wrongly detect halite pixels as gypsum. For the chlorophyll-a sensitive indices, the NDWI results are used to isolate the data to water pixels prior to processing.

All final index results are exported as single-band images and all of the unmasked/output pixels are used to determine the surface area extent of each class. Area calculation of each class result requires the use of GEE specific area functions to account for the projection of each pixel and calculate the geodesic area of each unmasked pixel. Area calculations without accounting for projection are greatly overestimated. All pixel-areas of unmasked pixels for each index result are summed together to estimate the total area of the class. These results are stored and exported as tables for analysis. In contrast, for the KIVU and 2BDA chlorophyll-a indices, the mean value of all unmasked pixels is calculated for each arm to represent the relative chlorophyll-a concentrations.

Other Data, Issues, and Error

From the index results, the exposed lakebed area is estimated by summing the area of vegetation, halite, gypsum, and carbonate-muds/other, while the calculated exposed lakebed area is estimated by subtracting the water area from the total area of the respective arm of the lake. A calculated exposed lakebed area is also presented for true-color images before 1984, where the water area is manually delineated and subsequently subtracted from the total area. The modelled exposed lakebed area is calculated by subtracting the modelled water area from the total area for each region. Erodable exposed lakebed area is calculated by summing the area of the gypsum and carbonate-muds/other classes, as these sediment types are unconsolidated and potentially susceptible to eolian transport. It is assumed that halite and vegetation around the rest of the exposed lakebed aids in retraining sediments from eolian transport by adding a protective surface (Reynolds and others, 2007). However, it has been observed that salt crusts may also contribute to dust events if enough desiccation and/or wind occurs (Bucher and Stein, 2016).

Additional products presented derived from spectral results are lake area extent boundaries (shapefiles) from select images, as well as a historical halite classification map derived from summing all halite index results for the North Arm. Lake area extent shapefiles are produced using the output NDWI rasters in ArcGIS Pro, where the rasters are converted to shapefiles, boundaries are dissolved, and all features except the main water body are removed. The historical halite classification map is also produced in ArcGIS Pro by summing all pixel-cell values for all North Arm halite images, which effectively produces a historical occurrence map of halite crusts across the lakebed since 1984. The halite values were then classified by value to ten quantiles to form a decile classification map to better assess distribution patterns. Daily precipitation data are acquired from NOAA station USW00024127 at the Salt Lake City International Airport, which is situated proximal to the southern end of the lake. River discharge data for the Bear, Jordan – West, Jordan – East, and Weber rivers are taken from USGS stations 10126000, 10171000, 10170500, and 10141000, respectively. Each station is proximal to the lake and roughly represents the river-water influx into the lake system. Yearly-running-averages of Palmer Drought Severity Index (PDSI) data, a relative dryness/drought indicator using temperature and precipitation data, is acquired for the Great Salt Lake region from 1982-2020 from Climate Engine using the gridMET Drought (4km resolution) dataset. A polygon is used to define the general area of the Great Salt Lake system in Climate Engine and the mean PDSI value of all gridded pixels within the polygon is calculated then exported.

Although official cloud percentage metadata are used to filter out cloudy scenes, it is noted that over 30 scenes show excessive amounts of clouds and are removed from analyses. This poor performance of the cloud detection algorithm is shared between both Landsat and Sentinel products but is infrequent as it occurs in only about five percent of the total amount of images. Other issues such as snow, smoke, and surficial-cyanobacteria-growth are observed for a handful of images and those are also excluded from analyses. However, over 15 other Landsat images were excluded from analyses due to strange image artifacts, encompassing much of the water body, resulting in a plethora of missing pixels for some or all of the spectral bands. In total, the observations from 80 images are excluded from analyses.

Given the constraints and limits of manually being able to differentiate surface types from multispec-

tral satellite imagery, as well as the vast spatial and temporal scope of the study area, one of the only error assessments available is to assess the performance of water-body detection with manually derived comparisons. Three locations around the lake are chosen for two separate Landsat scenes, and for each region the waterbody is manually delineated and the area is calculated and compared to the area reported by NDWI for the same locations. The magnitude of difference between the results is used as a rough error metric, indicating a difference of <1% for deep waters and difference of ~4% for shallow waters such as the Farmington Bay. It is observed in many resulting images that when the water in Farmington Bay is shallow, NDWI has difficulty and typically underestimates the water area. The performance of the vegetation and halite results appear to be very robust in that there is clear separation from background values when assessing the resulting images. Additionally, it is worth noting that both indices use a conservative threshold and thus may slightly underestimate the total area of these classes, as it is observed for many images that there is a slight halo around regions of classified pixels with values that could be also included in the class-of-interest as they are well-separated from background values.

A temporal model of Great Salt Lake water area is also included as a comparator for water-body detection performance and as an additional source of data. The model is based on a univariate spline interpolation of published values for area vs elevation of the lake, and estimates area via lake elevation data from USGS water-station sites 10010000 and 10010100 (Robert, 2005; Robert, 2006). The modelled values are a rough estimate as the initial resolution of the lake area data is for every 0.5 ft of lake elevation. However, the interpolation strongly matches the USGS curve as the interpolation utilizes 15 breakpoints (4169, 4171, 4173, 4178, 4183, 4188, 4194, 4200, 4201, 4203, 4205, 4207, 4209, 4211, and 4214 ft; Figure S1). Sources of differences between the modelled and observed area values primarily stem from differences in the boundaries utilized. The USGS North Arm area data does not include the evaporation pond to the west, which is included in this study in analyses until 1994, and the USGS South Arm area data includes the large evaporation pond west of Stansbury island, which is not included in analyses from this study and accounts for significant differences between the model and NDWI up until the year 2000 (when the water elevation dropped below the level which would naturally inundate the evaporation ponds). Nonetheless, the model provides a useful comparison and shows robust agreement with the NDWI results.

RESULTS & DISCUSSION

Water and Exposed Lakebed Area Evolution

The resulting time series data show a stark evolution in the surface area of the lake that closely follows the trends from lake elevation data as well as the modelled surface area (Figure 3). Annual oscillations in lake level are observable for years with more than about three images, as confirmed by the lake elevation and modelled data (Figure 3a). Sentinel imagery have a much higher temporal resolution and capture annual oscillations in greater detail. After the year 2000, the image-derived and modelled water areas have strong agreement, where the weaker agreement is due to the modelled area including a portion of the South Arm salt pool areas for years prior to 2000. The observations between the Landsat and Sentinel platforms appear to agree well and show relatively little difference.

The water surface area for both arms of the lake increase drastically from the 1970's into the mid 1980's where the lake filled due to significant precipitation, then slowly decreases in time with only a handful of wet years to follow. For the Bear River Bay, the water surface area decreased alongside falling lake levels until the early 2000's when the modelled and observed water area began to diverge. The modelled water area suggests the Bear River Bay should have been absent of standing water Around 2005, but the observed area indicates an anthropogenically maintained water surface area between 200 and 500 km^2, with an average of 300 km^2. After 2005 the Bear River Bay water surface area no longer followed trends in lake elevation change. Since the maximum extent of 1986-1987, which closely resembles the estimated mean lake area in the absence of anthropogenic consumption (Wurtsbaugh and others, 2017), the total observed lake area has decreased from ~5,700 km^2 to ~2,590 km^2 during the summer months, a loss of ~45%. When considering just the North and South Arms, the observed lake area has decreased ~30% from ~3,400 km^2 to ~2,380 km^2 since 1979. The South Arm water area has responded greater to lake elevation change, losing >250 km^2 more than the North Arm since 1986, with the drying up of the shallow Farmington Bay being partly responsible. During lowstands the South Arm water area is seen to oscillate in greater amplitude compared to the North Arm water area, which is coincident with the South Arm being directly influenced by seasonal fluxes in river input and association with more shallow lakebed. However, during highstands, when the lake arms are closer to equilibrium in elevation, the water areas fluctuate similarly. In contrast, the water area

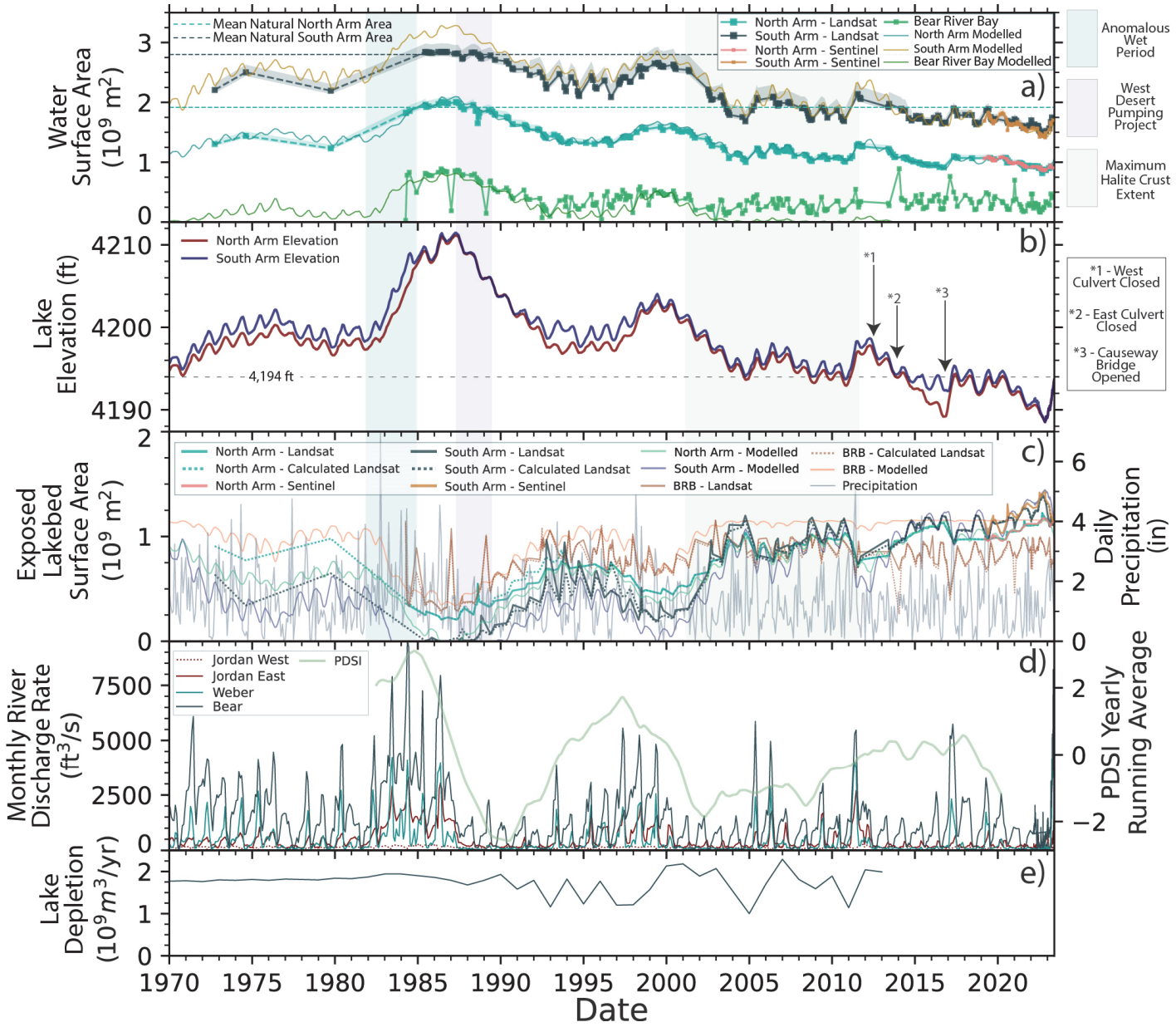

Figure 3. *Evolution of lake surface area (a), lake elevation (b), exposed lakebed surface area and daily precipitation (c), monthly river discharge rate and Palmer Drought Severity Index (PDSI) (d), and lake-input depletion data (e) (from Wurtsbaugh and others, 2017). The dashed horizontal lines on panel a) indicate the estimated natural mean area of each arm of the lake (corresponding to ~4,207 ft lake elevation) in the absence of anthropogenic consumption (Wurtsbaugh and others, 2017). The dashed horizontal line on panel b) indicates the 4,194 ft topographic threshold. Also included are color bars indicating times of the anomalous wet period (light blue), west desert pumping project (light purple), and maximum halite crust extents (light green). Error bars of -2.5% and +5% are used for lake surface area measurements, as it is more likely to underestimate the observation than overestimate. For the South Arm, between 1995 and 2015, the error bars show -2.5% and +10% due to the shallow Farmington Bay waters. The analyses do not include the North Arm salt pool after 1994. Arrows indicate specific events in time. The lake and exposed lakebed surface area panels (a, c) include remotely sensed area estimates and the modelled area derived from published surface area vs elevation calculations (Robert, 2005; Robert, 2006). Lake elevation data are from USGS water-stations 10010000 and 10010100. Daily precipitation data are from NOAA station USW00024127 at the Salt Lake City International Airport. Monthly river discharge rate data for the Bear, Jordan – West, Jordan – East, and Weber rivers are from USGS water-stations 10126000, 10171000, 10170500, and 10141000, respectively. PDSI data acquired from Climate Engine for the Great Salt Lake region.*

fluctuations within the Bear River Bay appear to follow greater seasonal and inter-seasonal variations, associated with seasonal flow variations for the Bear River and water-management actions.

For years with significant rains (Figure 3c), where the water elevation has been able to rebound multiple feet, the water area can be seen to dramatically increase, typically by 500-750 km^2, between the North and South Arms. For example, the wet year of 2011 increased the lake elevation by ~4 ft and North + South Arm area by ~670 km^2 (Figure 4). As the topography of the lake-bottom becomes significantly steeper below ~4,194 ft, water elevation changes below this elevation have significantly less impact to water area (Figure S1; Robert, 2005; Robert, 2006). Starting in 2003 the mean lake elevation began to fluctuate near 4,194 ft, which lasted until about 2020, and whenever lake elevation is seen to drop below ~4,194 ft there are noticeably less significant changes in water surface area. Knowing that the lake area is

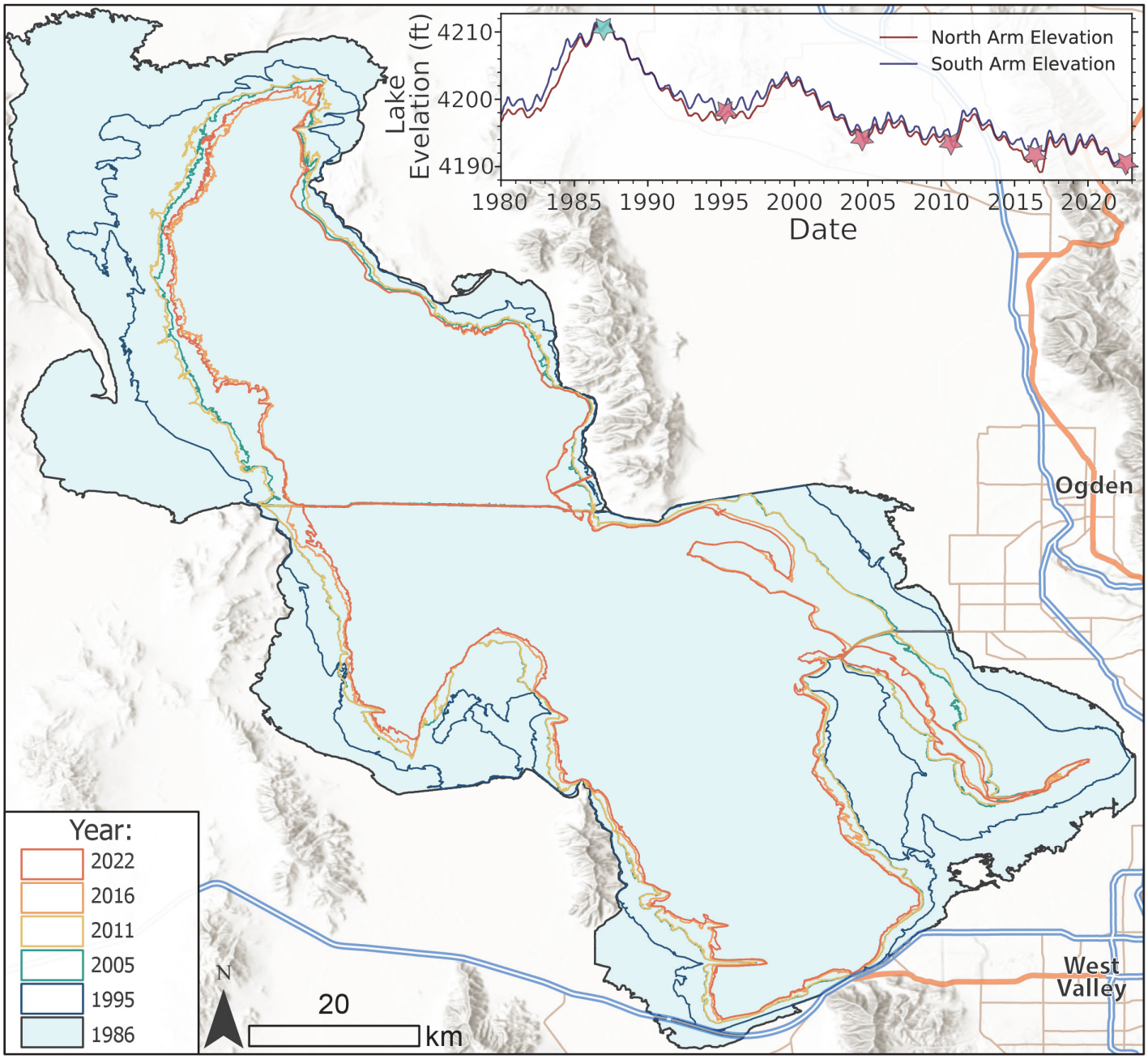

Figure 4. *Water boundaries of both the North and South Arms for all the major lowstands since 1986 (1995, 2005, 2011, 2016, and 2022) compared to the highstand boundary of 1986. The boundaries show the outermost boundary and do not include interior boundaries such as the boundaries along island perimeters. The southwestern North Arm evaporation pool is only included for the 1986 boundary and the Bear River Bay is not included. A lake elevation plot is inset in the upper right as reference, with the data being from USGS water-stations 10010000 and 10010100. The basemap is the ESRI World Hillshade map with an ESRI highway layer. The 2005 and 2011 boundaries are close to the ~4,194 ft threshold.*

more sensitive to lake elevation above ~4,194 ft indicates that lake managing efforts should aim to keep the lake at least above ~4,194 ft to maximize the area of the lake and sediment coverage. Ideally, when considering maximizing water area (sediment coverage), the water elevation should be kept above ~4,200 ft so fluctuations don't drop near the ~4,194 ft threshold. Maximizing sediment coverage will be increasingly important in the future to mitigate more-significant dust events. A recent report for policymakers determined the optimal range of lake elevation is between 4198 and 4205 ft, with a transitionary zone between 4195 and 4198 ft, based on impacts to air quality, ecosystem, mineral production, recreation, and brine shrimp viability (Ahmadi and others, 2023). These proposed elevations align with the presented minimum threshold of ~4194 ft, and if implemented would result in a North + South Arm lake area of ~3,100 to ~4,700 km^2, roughly 700 to 2,300 km^2 greater than the lake area in 2022.

Associated with the lake surface area change, the total observed exposed lakebed area has increased ~2,985 km^2, from ~504 km^2 to ~3,489 km^2 over 36 years (Figure 3c). Assessed as a simple trend, this suggests the rate of exposed lakebed area growth has been roughly 80 km^2 per year. Compared to 1979, before the significantly wet period, the exposed lakebed area for the North and South Arms has increased ~1,000 km^2, from ~1,600 km^2 to ~2,600 km^2. Since 1986-1987 the South Arm has exposed nearly 50% more exposed lakebed compared to the North Arm, as the South Arm has had a stronger response to water level dropping. However, much of this additional exposed lakebed, particularly in Farmington Bay, has been altered from a saline mudflat to a vegetated wetlands ecosystem with the rapid encroachment of phragmites. Erodable exposed lakebed, exposed lakebed without vegetation or halite crusts to entrain the sediments, has increased from ~330 km^2 to ~2,750 km^2 since 1986-1987 for the total lake system. Erodable exposed lakebed increased by ~900, ~1,110, and ~390 km^2 for the North Arm, South Arm, and Bear River Bay, respectively, since 1986-1987. The Bear River Bay has had much less of an increase in erodable exposed lakebed due to anthropogenic maintenance of surface waters and the smaller size of the subsystem area. Although vegetation and halite help to protect a sizable portion of the exposed lakebed surface, erodable exposed lakebed has consistently dominated more than 80% of the exposed lakebed surface, except for Bear River Bay where the average proportion of erodable lakebed surface has been roughly 60%. A caveat associated with vegetation growth protecting the surface is that much of the vegetation in the South Arm is due to invasive Phragmites, which consume significant amounts of water compared to native vegetation (Kulmatiski and others, 2011).

Precipitation and river discharge data (Figure 3c-d) help explain major changes to water and exposed lakebed area, where years with significant rains typically result in a much greater river discharge which significantly increase water area and decrease exposed lakebed area. However, years with higher amounts of precipitation but no increase in river discharge (i.e., 2002, 2003, and 2015), associated with river diversion/extraction for agricultural and other uses (Figure 3e), are seen to have little effect on the lake/exposed lakebed area (Wurtsbaugh and others, 2017; Ahmadi and others, 2023). Thus, although precipitation directly impacts river discharge, if consumption of the river waters is too great there may be no increase in water/exposed lakebed area and perhaps a decrease. Utilizing a yearly-running-mean of the Palmer Drought Severity Index (PDSI) emphasizes wetter and drier periods, effectively separating periods with low and high river discharge connected to climatic cycles (Figure 3d). The PDSI values of the mid-1980's and late 1990's are indicative of wetter periods (>1), which is clear from precipitation and river discharge data, but the mid-2010's are indicated to be transitional (~0) although discharge into the lake was relatively low. In general, trends from PDSI follow trends from lake elevation and area well up until ~2013, where infrequent but significant precipitation caused the PDSI to slightly rise but the lake elevation and area continued to decline.

Exposed Lakebed Evolution

Results from the spectral indices for vegetation, halite, gypsum, and carbonate-muds highlight key similarities and differences between the North Arm, South Arm, and Bear River Bay (Figure 5). Sentinel and Landsat surface classifications agree well, although there are noticeable differences during 2022 where Sentinel appears to underestimate the vegetation and evaporite extent. The most significant difference between the sediments shared between the lake regions is that the extent of evaporite formation is magnitudes greater in the North Arm (Figure 5a-e). Carbonate-muds comprise the majority (>75%) of the exposed lakebed for all lake regions and vegetation is typically the second most prevalent land cover type. Through the temporal evolution of exposed lakebed area, the percentage of each surface type appears to stay relatively consistent through time, in that there haven't been any significant changes to the proportion of sediment types as the lake has rapidly

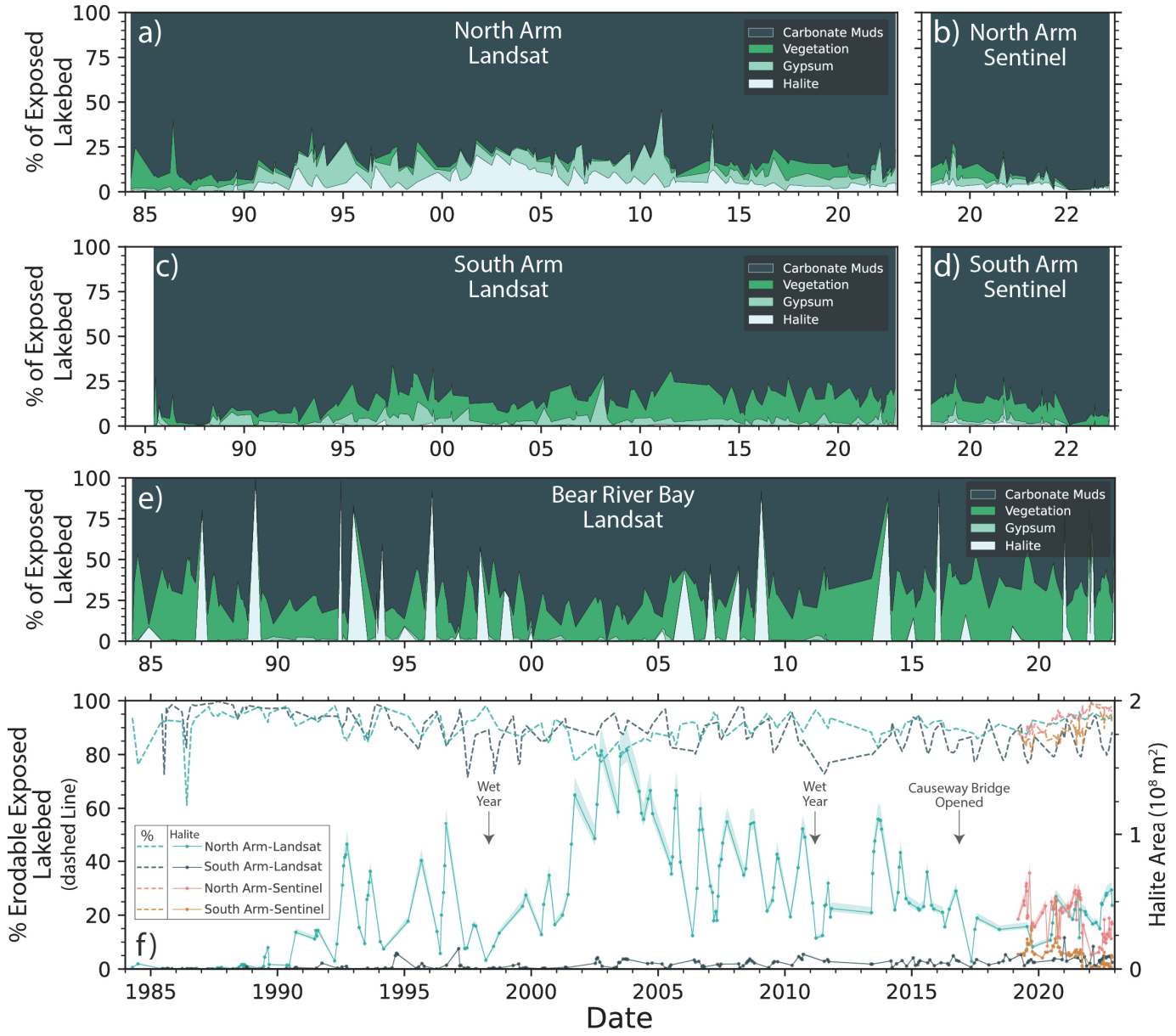

***Figure 5**. Percentage of each surface type for the North Arm (a-b), South Arm (c-d), and Bear River Bay (e) exposed lakebed areas, split between Landsat (a, c, e) and Sentinel (b, d) observations, as well as the percentage of erodable exposed lakebed area and detected halite area for the North and South Arms (f). The dashed line on f) indicates the percentage of erodable exposed lakebed.*

dropped. This is also observed through temporally assessing the percentage of erodable exposed lakebed (Figure 5f – dashed line) which consistently oscillates between ~75-95% of the exposed lakebed area for the North and South Arms. Seasonal oscillations in extent for vegetation and evaporites coincide with wet/cold and dry/warm seasons, as seen by the annual fluctuations of exposed lakebed land cover proportions by ~5-20%. Seasonal variation in halite extent appears to be greatest for the Bear River Bay, as there are spikes of halite detection during the winter months when the surface waters are at a minimum extent (Figure 5e). However, the halite variations in the Bear River Bay are likely overestimated by the sensor as the values appear unreasonably high. Overall, evaporites appear to be lesser occurring in Bear River Bay as compared to the North and South Arms, and minimally contributes to the Bear River Bay lakebed outside of winter months.

Halite crust formation has been a significant part of the evolution of the North Arm exposed lakebed area (Figure 5a,f). Halite crust in the North Arm is formed from either evapoconcentrating pore-waters of surficially saturated sediments or by precipitation of halite in the supersaturated lake waters and accumulation on the lake-bottom. Spanning much of the North Arm lake-bottom is a robust and thick (>1 ft) halite crust, which becomes partially exposed around the perimeter of the water when the lake recedes (Rupke and others, 2016; Rupke and Boden, 2020). Additionally, during the warmer months the waters and saturated sediments on and/or near the fringe of

the water-sediment-interface commonly reach halite supersaturation through evapoconcentration, or are already supersaturated, and form halite crusts that vary in extent depending on a variety of factors (Jagniecki and others, 2021). From the satellite observations, the greatest observed extent of halite in the North Arm is roughly 150 km^2, in contrast to the greatest observed extent of halite in South Arm of roughly 30 km^2. However, the temporal evolution of halite crust extent in the North Arm is complex and the average extent of halite since 1990 is ~78 km^2. Seasonal fluctuations in halite crust area can vary in magnitude but it is common to see changes greater than 50 km^2 during the wet and cold months when halite crusts dissolve and/or when sediments wash in and mask the crust surface.

Gypsum extent appears to be independent of halite formation, as gypsum extent is observed to vary regardless of halite. However, gypsum extent follows seasonal variations where the greatest extent is during the colder and wetter months, and is most prevalent in the North Arm, despite that active gypsum precipitation of significant amounts is unlikely to occur from lake waters. These observations may be attributed to seasonal coverage/reworking by loose sediments or halite crusts, detecting other hydrated sulfate rich minerals (such as mirabilite), or annual cycles of gypsum precipitation from springs or interstitial brines (Jagniecki and others, 2021). Significant aggregates of mirabilite, if present, are likely classified as gypsum, as their mineralogy and spectral characteristics are similar (Kokaly and others, 2017). As gypsum observations are greatest in winter when mirabilite is known to form in the Great Salt Lake system, it is reasonable to interpret that the observations are indeed incorporating detections of mirabilite, which suggests the variations are less in part due to variations in gypsum distribution but rather variations in the combined distributions of gypsum and mirabilite. It is likely a significant portion of the surficial gypsum at a given time is retained from previous years due to redistribution to drier, more protected zones. Redistributed gypsum may also be a by-product of evaporative mining in the system. Although the South Arm forms few halite crusts, gypsum spatiotemporally accounts for an appreciable portion of the exposed lakebed surface, which may be a valid observation or indicate the gypsum threshold is too low as the reported amounts of gypsum are unexpectedly significant. Observations from Bear River Bay indicate a minimal presence of gypsum, a finding that is consistent with the bay's fresher water qualities but may also be associated with local geology, biological mediation, and/or hydrologic processes.

Vegetation in the Great Salt Lake system spread dramatically starting in the early 1990s, where vegetation in the South Arm and Bear River Bay started growing with rates of ~9 and ~11 km^2 per year, respectively (Figure 6a). The areas of greatest vegetation growth are associated with the Farmington and Bear River bays, with the Bear River Bay hosting the most vegetation. The Bear River Bay hosts a variety of agricultural, wetland, and floodplain vegetation types while the Farmington Bay mainly hosts wetland vegetation types. The greatest seasonal variations in vegetation area are attributed to Bear River Bay, which can vary over 300 km^2 (up to >90%) from summer to winter, with the South Arm also showing significant seasonal variations. In 2020 the area of vegetation in the Bear River Bay spiked over 500 km^2, 340+ km^2 (>300%) greater than pre-1995 observations of vegetation area. The area of vegetation in 2022 is ~400+% greater than the area of vegetation between 1984-1994. Vegetation in the North Arm shows no significant growth up until around 2010, when vegetation started growing rapidly and quadrupled in area in about 6 years. However, since 2019 the extent of vegetation in the North Arm has dropped dramatically. NDVI comparisons between Landsat and Sentinel agree extremely well, possibly better than any of the other indices used in this study. Overall, satellite observations suggest vegetation is rapidly encroaching on the exposed lakebed of the Bear River Bay and Farmington Bay.

Chlorophyll-a analyses represent the mean relative chlorophyll-a concentration for each arm of the lake and shows much different temporal results for both arms of the lake (Figure 6b-c). Although the microbiology of both arms is greatly different and that many of the organisms don't produce chlorophyll-a but produce carotenoids (a different biotic pigment), it is expected the chlorophyll-a indices should still capture changes in pigment (Weimer and others, 2009; Roney and others, 2009; Baxter, 2018). The North Arm shows a continual decrease in relative chlorophyll-a concentrations through time, having the greatest decreases between ~1992-1995 and ~2012-2013 (Figure 6b). In contrast, the South Arm shows a relatively consistent average chlorophyll-a concentration that fluctuates seasonally with variations in temperature, nutrient flux, and turbidity (Figure 6c).

Sentinel 2BDA results, which are likely more sensitive to true chlorophyll-a changes due to the inclusion of a red-edge band, capture large seasonal chlorophyll-a fluctuations in the South Arm that are much greater in amplitude than changes in the North Arm. Given that the salinity of the North Arm is much greater than the South Arm due to a lack of inputs, and that turbidity is much lower in the South Arm, the biotic regime is known to be much different and ex-

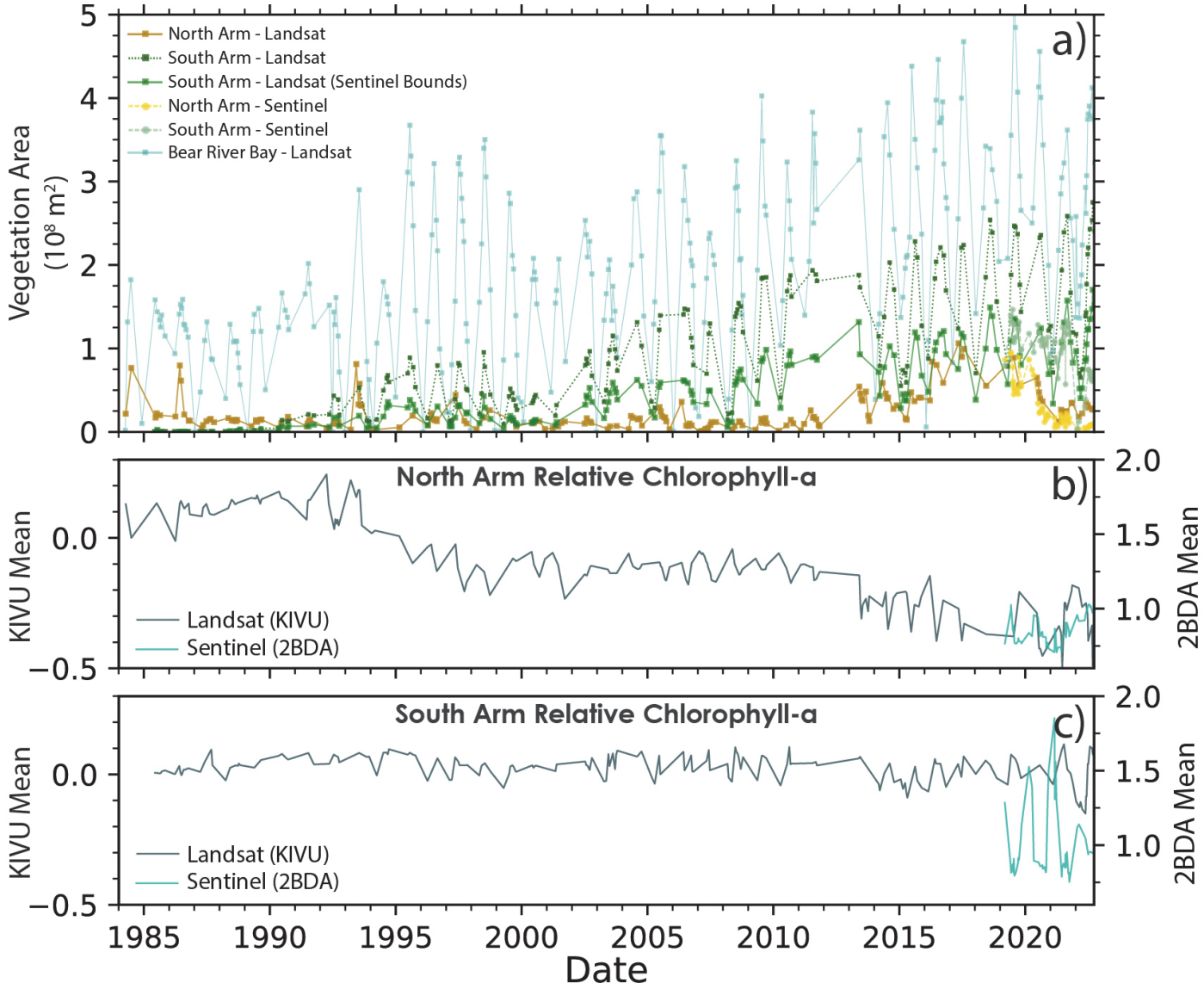

Figure 6. *Evolution of vegetation area (a) for each region of the Great Salt Lake and mean relative chlorophyll-a concentrations for the North (b) and South (c) Arms from both Landsat and Sentinel data. The dark green line of panel a), labeled "South Arm – Landsat (Sentinel Bounds)" shows the area of vegetation in the South Arm for Landsat data that are clipped to the extent/boundary of the Sentinel-2 imagery for direct comparison.*

plains the differences between the lake arms. Reasoning to explain the continual decline of chlorophyll-a in the North Arm is that in the 1980s when the lake filled the salinity dropped drastically, nutrient flux increased, and turbidity increased all leading to conditions favorable for microorganism growth. As the North Arm has evolved to be more saline, the microorganism community transitioned to saline-favorable organisms and subsequently the less halotolerant microorganisms died (Almeida-Dalmet and others, 2015; Baxter, 2018). Additionally, it has been observed that the modern community of microorganisms in the North Arm is more resistant to changes in salinity and temperature than in the South Arm (Almeida-Dalmet and others, 2015), which may explain the slower rate of observed changes between 1995 and 2013 as well as the smaller magnitude of seasonal changes in the North Arm. The Landsat and Sentinel results agree well for changes in chlorophyll-a concentration in the North Arm but appear inversed for the South Arm, which may be due to environmental noise or the limitations of the Landsat TM and OLI sensors to observe changes in chlorophyll-a response of the microorganisms present in the South Arm.

Evolution of Halite Crusts

Exposed halite crusts in the North Arm were nonexistent during the highstand following the mid-1980s but started forming or becoming exposed in the early 1990s (Figure 5f). Overall, it appears halite crusts grow in extent as lake levels recede to lowstands (1995, 2004, 2010, 2015, and 2022) and when there is moderate-to-significant annual variations in water surface area (annual redistribution of saline waters to

sediment-pore-spaces). In contrast, the halite crusts appear to shrink during periods of wet seasons or extended exposure. Following a wet season that dissolved most of the halite crusts in 1998, the lake reached a highstand in 2000 then slowly receded where halite crusts subsequently reached a maximum extent of ~163 km^2 in October 2002 and 2003. Following 2003 the extent of halite crusts slowly dropped until another wet year during 2011, which quickly diminished halite extent and was followed by receding lake levels through 2016. Halite crusts grew again in 2013 to extents similar between 2005-2010 but then started shrinking to the lowest extent in roughly 20 years in 2017. Since 2017 halite crusts have been slowly growing again, increasing in size leading up to the lowstand of 2022, but are roughly half the size of crusts observed between 2005-2010 and a quarter of the maximum extent.

Changes in halite crust extent are observed to partially correspond to significant water management changes. In 2012 the western culvert allowing for flow between the South and North Arm was closed and similarly in 2013 the eastern culvert was closed (Figure 3b and 5f). The closure of both culverts led to a drop in lake elevation for the North Arm of greater than 5 ft as the North Arm no longer had any major water input. The rapid drop in lake elevation would have led to exposure of nearshore salt crusts that were previously under water, which is likely responsible for the increase in halite crust area in 2013. Subsequent rain and sheetflow events would have progressively dissolved the exposed lake-bottom halite crust, as seen from 2013 to 2016. In late 2016 a causeway bridge was opened to resume flow into the North Arm, which resulted in a rapid increase in water elevation and dilution of the North Arm water salinity (Jagniecki and others, 2021). The significant decrease in halite extent during the early summer of 2017 is likely due to the mixed contribution of rapid water level increase and the influx of fresher waters. Rapid water level rise, where the lake rose several feet over the course of a few months, would have inundated and/or dissolved nearshore halite crusts, and fresher water influx undersaturated the water with respect to halite leading to halite dissolution. Waters appear to have reached halite saturation by late 2017 into early 2018 as halite crusts reappear (Figure 5e). These observations indicate that water management, specifically managing the flow from the South Arm to the North Arm, has a large impact on halite crust formation processes.

Aside from direct precipitation (meteoric rain and snow), inundation, and water management, mirabilite formation driven by cold temperatures may be partly responsible for the decreases in halite crust extent, specifically for years where the winter months provided little precipitation but the halite extent dropped significantly. Reports have identified that during the colder months mirabilite precipitates from the North Arm water column and effectively lowers the salinity of the water to the point where the water becomes undersaturated with respect to halite (Jagniecki and others, 2021). This process may cause the lake water and sediment-pore-water to dissolve halite crusts along the shoreline during the winter months, even in the absence of precipitation.

Spatial Distribution of Surface Types

Although the time series results provide valuable information regarding the overall evolution of the lake system, the classification map results help understand the distribution of the surface types, which is useful for interpreting the processes responsible for shifts in exposed lakebed composition and cover. The classification results for the North Arm show that during the highstand of the 1980s when lake levels were very high there is little exposed lakebed exposed, but what lakebed is exposed is associated with a significant amount of vegetation (Figure 7a). Following this time, the lake declined rapidly into the 1990s where significant exposed lakebed area appears with sizable halite crusts focused on the northwest sector of the exposed lakebed and much less vegetation (Figure 7b). The halite crusts during this period extend roughly 1-4 km from the shoreline and show a close association to proximal gypsum deposits that are likely underlying much of the halite. Gypsum appears most prevalent in the North Arm during the 1990s but also reappears in similar extent in later years (Figure 7b,c,h). The classification maps from 2002 and 2006 show some of the greatest extents of halite, where the map from 2002 shows halite at its near-maximum extent with crusts on average extending 5 km from the shoreline on the western side (Figure 7d). Additionally, during this period sizable crusts are observed on the eastern side near the location of the Spiral Jetty. Although the lake area in 2011 rebounded to near the 2002 extent, the distribution of halite crusts during and after 2011 is dramatically less and is limited to about 1-2 km from the shoreline (Figure 7f). This suggests that the majority of exposed halite crusts in the North Arm are formed as part of the lake-bottom crust rather than evapoconcentration of saturated sediment-pore-water, and that the lake-bottom crust didn't have suitable time or conditions to grow near the 2002 extent during the highstand of 2011. In 2017 the vegetation in the North Arm is seen to grow dramatically and the water area decreased, along with a thin

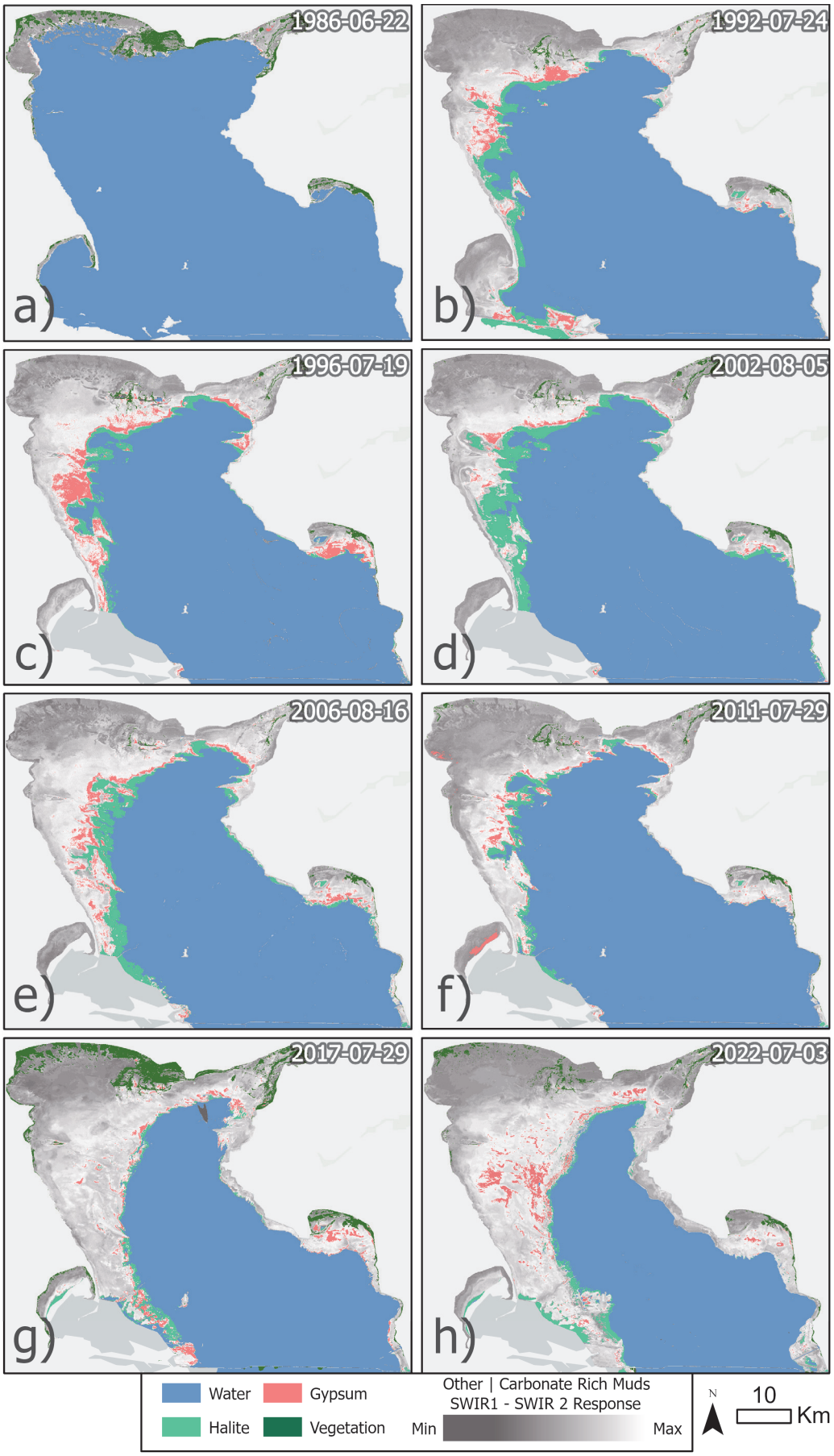

Figure 7. *North Arm classification maps illustrating surface type distributions during 1986 (a), 1992 (b), 1996 (c), 2002 (d), 2006 (e), 2011 (f), 2017 (g), and 2022 (h).*

extent of halite along the western perimeter of the shoreline (Figure 7g). The 2022 classification is similar, with a further decline in water extent but perhaps somewhat more halite distributed about the shoreline as well as on the outside perimeter of the salt ponds to the southwest (Figure 7h). However, the vegetation growth observed in 2017 is absent in 2022 and there is significantly more distributed gypsum to the northwest.

In general, as the water elevation and water area decreased, the halite has been focused around the western side of the North Arm shoreline and crusts have slowly fallen in elevation and extent alongside the lake. It is likely that the shallow slope of the lakebed on the western side of the North Arm has contributed to the greater observed extents of halite crust. A historical halite distribution map, produced by summing all halite images in the North Arm and classifying the image using deciles (ten quantiles), emphasizes the lateral migration of halite crusts through time as the areas where halite crusts repeatedly formed on the western side have much greater values (recurrence of detections) than the surrounding landscape but extend nearly 10-15 km from the modern shoreline (Figure 8). Recent crusts, which rim the water boundary, show up within the lower decile classes, reflecting less recurrent observations of halite in those areas since 1984. Spherical-to-ellipse shaped zones with high pixel values ($\geq 80^{th}$ decile) on the western side may be local lows that promoted halite crust formation through ponding. Although the western side has been the predominant location for halite crust formation, the map shows that halite crusts have formed along the entire shoreline since initial exposure in 1990. Years with the most halite appear to correspond to years where there has been a sustained drop from higher-to-lower water elevations exposing the robust lake-bottom crust and/or where the water elevation is above ~4,194 ft such that the exposed lakebed slope is shallower. When the water levels seasonally fluctuate above ~4,194 ft a broader area of sediments can become saturated with saline waters, which should result in more expansive halite crust formation during the summer months when evapoconcentration of sediment-pore-water can form a thin halite crust on the surface. This effect may explain why recent halite crusts have been much smaller than the crusts observed between ~1995-2013, as the water elevations have been on average below ~4,194 ft and the seasonal water area fluctuations are much less. Alternatively, the opening of the new causeway breach in 2016, which allows for much greater south-to-north flow, could be responsible for the smaller recent crusts, as the waters significantly dropped in salinity and have been slowly recovering. Both seem reasonable explanations that can occur in conjunction, however, it appears lake-bottom crust temporally composes the majority of exposed North Arm halite crust. Thus, the new causeway has likely had a greater impact on recent halite crust formation/exposure than changes to seasonal redistribution of saline waters to sediment-pore-spaces.

In contrast to the North Arm, classification results for the South Arm show a much different distribution of sediment types and vegetation. In 1986 the South Arm was very full (Figure 9a) but decreased significantly into the 1990s, leading to lakebed exposure and the start of vegetation growth in the Farmington Bay region (Figure 9b-c). Relatively little halite is observed in the South Arm during the 1990s except for a small crust and associated gypsum to the south. The 2002 and 2006 classification maps (Figure 9d-e) show the initial decline of Farmington Bay waters and indicate some small halite crusts to the south. In 2006 there is a significant increase in gypsum extent that appears to be linked to the gypsum distributions through 2017 (Figure 9e-g). The 2011 map shows a significant increase in water and vegetation area, but also highlights water detection issues in the shallow and turbid Farmington Bay as some of the water area is classified as carbonate-muds and vegetation (Figure 9f). The maps from 2017 and 2022 (Figure 9g-h) show drastic reductions in water area for the Farmington Bay alongside slight vegetative growth and a somewhat significant halite crust to the south that is roughly 5 km long and 2 km wide. The water elevation and area during 2022 was the lowest ever recorded. The 2022 classification map also shows errors for shallow and turbid water detection as the outer lateral sides of the water in the Farmington Bay (now in a channel) are detected as carbonate-muds (Figure 9h).

CONCLUSIONS

This study processed over 600 reflectance satellite images to better understand the evolution of the water, vegetation, halite, gypsum, and carbonate-mud land cover types in the Great Salt Lake system from 1984 to 2023. The results highlight the magnitude and pace of changes in the system, showing that the exposed lakebed area and halite crust area has responded significantly to lake elevation changes through time. Since 1986-1987 the total lake area has decreased by ~45%, from ~5,700 km^2 to ~2,590 km^2 during the summer months, where the South Arm has decreased in greater extent than the North Arm. Likewise, the exposed lakebed area has increased by ~2,985 km^2 over 36 years and reached an area of over ~3,489 km^2 in 2022. The Bear River Bay followed a natural decline in water area up until ~2000, when the

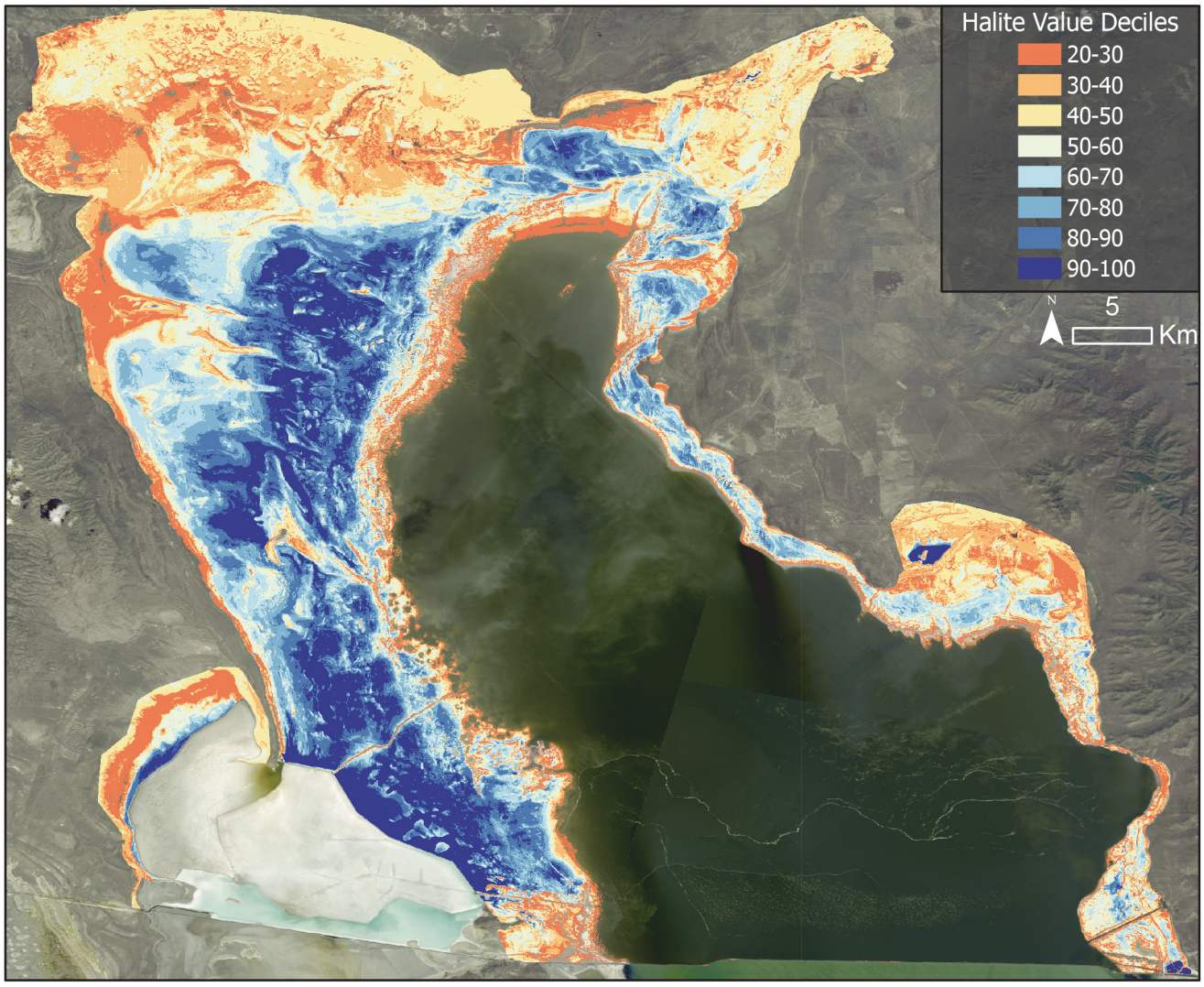

Figure 8. *Decile classification raster produced from the summation of all North Arm halite pixel cells between 1984 and 2023, showing the historical halite distribution and areas with most-or-least recurrent halite crusts. Values are separated into ten quantiles (deciles), where the largest decile indicates the greatest summation of halite values and the most common historical sites of halite formation. Modern halite crust locations, confined near the water boundary, have had significantly fewer recurring observations and are classified in lower deciles. The basemap is Landsat 8 OLI imagery from June 1st (south image) and 2nd (north image).*

water area diverged from the natural evolution to be anthropogenically maintained near an average surface area of ~300 km^2.

The critical elevation of ~4,194 ft, where there is a shift in the topographic slope of the lake-bottom, has a sizable impact on the magnitude of water/exposed lakebed area changes and should be of importance to land-managers and law makers associated with the management of the Great Salt Lake. Above ~4,194 ft the lake responds much more significantly to changes in elevation, such that the water area increases significantly even for small changes in water elevation. This is not only important to maintain a healthy size of the lake but to promote evapoconentrative halite formation in saturated sediment-porewaters, as it appears halite crusts have formed in more distributed amounts when the lake fluctuates in elevation above ~4,194 ft and effectively saturates more sediments with a saline brine. Furthermore, a greater extent of lake waters promotes expanded lake-bottom halite crust formation, which would be exposed when lake levels recede. Years with significant river discharge into the South Arm, which can sometimes be associated to years with lower river water consumption rather than higher amounts of precipitation, are observed to rapidly and significantly increase the water surface area, typically by 500-750 km^2. This suggests that water conservation efforts, that would lead to a greater annual river discharge into the Great Salt Lake, have the potential to significantly increase the surface area of the lake.

Halite crusts are predominantly observed in the North Arm, where the extent of crusts has undergone a complex evolution since the 1980's. The maximum extent of halite occurred between 2002 and 2003 in the North Arm, with crusts extending over 150 km^2.

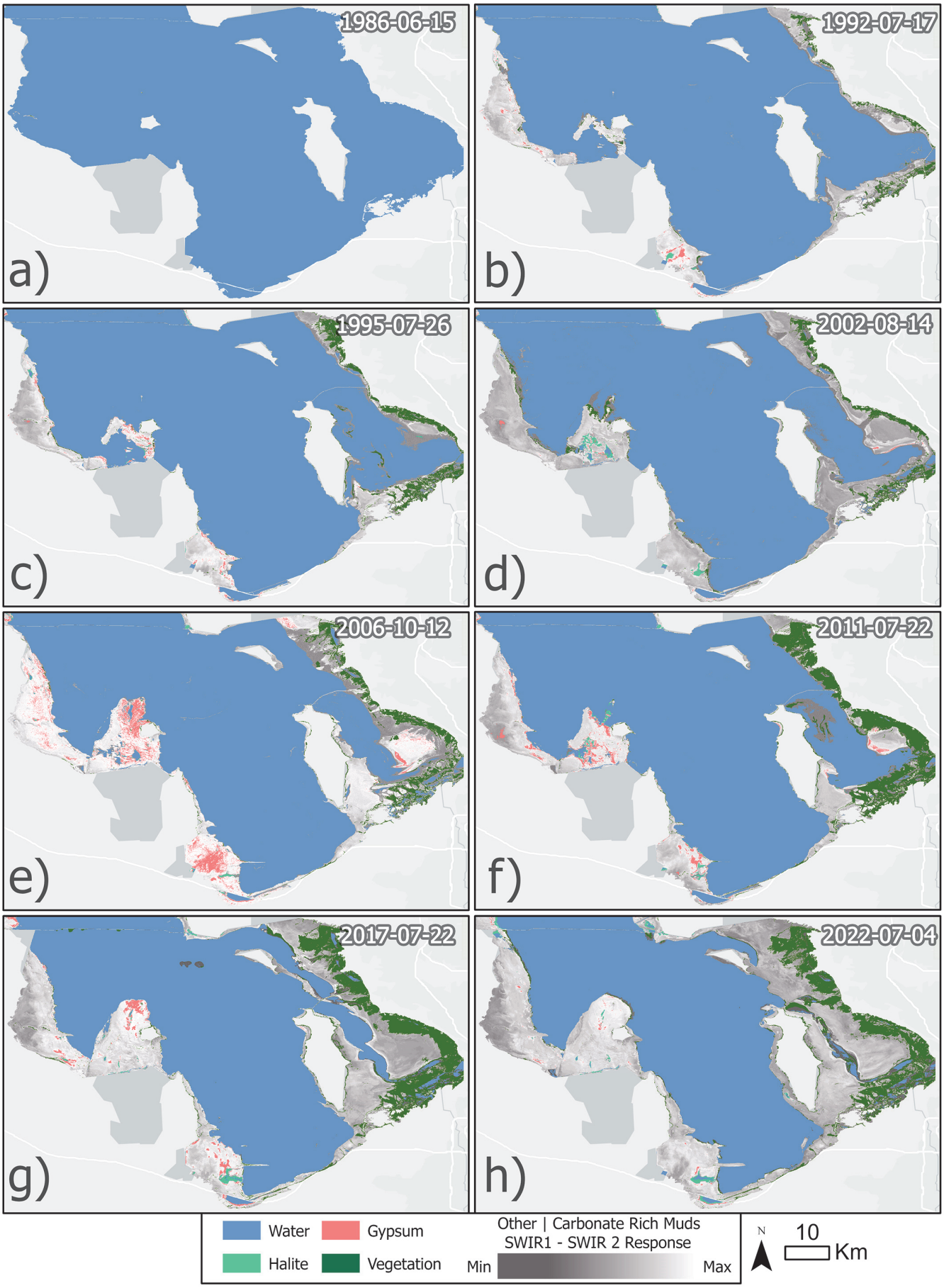

Figure 9. *South Arm classification maps illustrating surface type distributions during 1986 (a), 1992 (b), 1995 (c), 2002 (d), 2006 (e), 2011 (f), 2017 (g), and 2022 (h).*

Since the peak extent halite crusts have significantly shrunk, related to changes in land-use, lake elevation, and annual fluctuations. The most important control over halite extent appears to be associated with the lake-bottom crust formation/accumulation, topography, and magnitude of seasonal fluctuations. Periods of elevated water levels facilitate the restoration and expansion of the lake-bottom halite crust. Subsequent receding water levels then enable the exposure of these crusts. Greater seasonal elevation fluctuations and shallower topography leads to broader sediment saturation and evapoconcentrative halite crust formation. Other important controls that may have impacted the extent and distribution of halite crusts is management of the causeway, where management has affected the salinity and water levels of the North Arm waters. Additionally, results from this study are consistent with recent findings in the North Arm of forced halite dissolution by mirabilite precipitation in cold temperatures, such that there are significant seasonal variations of halite extent even for winters with relatively little precipitation to dissolve the expansive halite crusts.

Overall, remote sensing techniques to monitor the Great Salt Lake system have been established in this study and provide valuable observations that should be used in conjunction with other monitoring campaigns in the future. Future studies should utilize ground truth missions using spectroradiometers and drone surveys to quantify errors using these spectral techniques as well as provide further information on the modern land cover types. Similarly, the use of multispectral and active-radar satellites in future studies may help differentiate vegetation types in the Great Salt Lake system.

SUPPLEMENTAL DATA

The results of the analyses, including supplemental data such as a list of outlier images not used for analyses and the NDWI thresholds for each Landsat image, as well as satellite imagery based videos animating the evolution of the lake, are stored on an online database: https://doi.org/10.5281/zenodo.7996314 or https://zenodo.org/record/7996314

Code utilized in this study for data retrieval and modelling can be found on GitHub: https://github.com/radwinskis/Great-Salt-Lake-2023-Study-Code

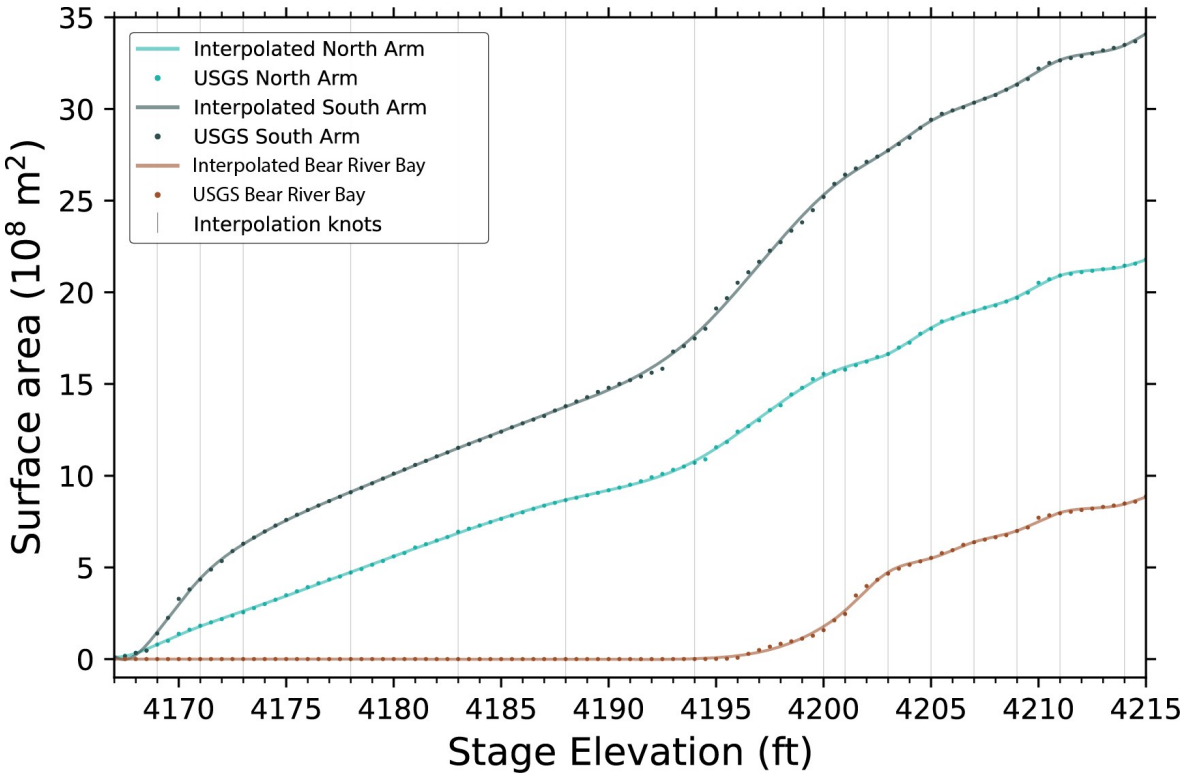

Figure S1. *Hypsometric data and curves for the North Arm, South Arm, and Bear River Bay as shown by published USGS data (dots) and interpolations of the USGS data (solid lines), illustrating the changes in surface area compared to changes in elevation, which is related to the topography of the lake-bottom. The ~4,194 ft threshold is easily seen where the slope of the lines change between 4190 and 4200 ft. From ~4,195 to ~4,201 ft the slope is much steeper, which indicates between these elevations the topography is much shallower. The interpolated lines are formed using 15 breakpoints shown as gray vertical lines. The data and interpolations show to fit very well, supporting the use of interpolation to model lake surface area.*

REFERENCES

Ahmadi, L., Albers, E., Bingham, B., Brooks, P., Endter-Wada, J., Hasenyager, C., Lin, J., McEntire, A., Neilson, B., Null, S., Perry, K., Stireman, B., Strong, C., Vernon, L., and others, 2023, Great Salt lake policy assessment – a synthesized resource document for the 2023 General Legislative Session: Great Salt Lake Strike Team Great Salt Lake Policy Assessment.

Almeida-Dalmet, S., Sikaroodi, M., Gillevet, P., Litchfield, C., and Baxter, B., 2015, Temporal study of the microbial diversity of the north arm of Great Salt Lake, Utah, U.S.: Microorganisms, v. 3, no. 3, p. 310–326 (doi: 10.3390/microorganisms3030310).

Amani, M., Ghorbanian, A., Ahmadi, S.A., Kakooei, M., Moghimi, A., Mirmazloumi, S.M., Moghaddam, S.H.A., Mahdavi, S., Ghahremanloo, M., Parsian, S., Wu, Q., and Brisco, B., 2020, Google Earth engine cloud computing platform for remote sensing big data applications – a comprehensive review: IEEE Journal of Selected Topics in Applied Earth Observations and Remote Sensing, v. 13, p. 5326–5350 (doi: 10.1109/JSTARS.2020.3021052).

Arnow, T., 1984, Water-level and water-quality changes in Great Salt Lake Utah, 1847-1983: U.S. Geological Survey Circular 913, 22 p.

Baskin, R.L., 2005, Calculation of area and volume for the south part of Great Salt Lake, Utah: U.S. Geological Survey Open-File Report 2005-1327.

Baskin, R.L., 2006, Calculation of area and volume for the north part of Great Salt Lake, Utah: U.S. Geological Survey Open-File Report 2006-1359.

Baxter, B.K., 2018, Great Salt Lake microbiology: a historical perspective: International Microbiology, v. 21, no. 3, p. 79–95 (doi: 10.1007/s10123-018-0008-z).

Bowen, B.B., Kipnis, E.L., and Raming, L.W., 2017, Temporal dynamics of flooding, evaporation, and desiccation cycles and observations of salt crust area change at the Bonneville Salt Flats, Utah: Geomorphology, v. 299, p. 1–11 (doi: 10.1016/j.geomorph.2017.09.036).

Bradt, S., Wurtsbaugh, W.A., Naftz, D., Moore, T., and Haney, J., 2006, Remote sensing as a tool to track algal blooms in the Great Salt Lake, Utah, USA [abs.]: American Geophysical Union Fall Meeting Abstracts, abstract H52A-04.

Bucher, E.H., and Stein, A.F., 2016, Large salt dust storms follow a 30-year rainfall cycle in the Mar Chiquita Lake (Córdoba, Argentina): PLOS ONE, v. 11, no. 6, p. e0156672 (doi: 10.1371/journal.pone.0156672).

Buma, W.G., and Lee, S.-I., 2020, Evaluation of Sentinel-2 and Landsat 8 images for estimating chlorophyll-a concentrations in Lake Chad, Africa: Remote Sensing, v. 12, no. 15, p. 2437 (doi: 10.3390/rs12152437).

Carling, G.T., Fernandez, D.P., Rey, K.A., Hale, C.A., Goodman, M.M., and Nelson, S.T., 2020, Using strontium isotopes to trace dust from a drying Great Salt Lake to adjacent urban areas and mountain snowpack: Environmental Research Letters, v. 15, no. 11, p. 114035 (doi: 10.1088/1748-9326/abbfc4).

Crosman, E.T., and Horel, J.D., 2009, MODIS-derived surface temperature of the Great Salt Lake: Remote Sensing of Environment, v. 113, no. 1, p. 73–81 (doi: 10.1016/j.rse.2008.08.013).

Drusch, M., Del Bello, U., Carlier, S., Colin, O., Fernandez, V., Gascon, F., Hoersch, B., Isola, C., Laberinti, P., Martimort, P., Meygret, A., Spoto, F., Sy, O., Marchese, F., and Bargellini, P., 2012, Sentinel-2 – ESA's optical high-resolution mission for GMES Operational Services: Remote Sensing of Environment, v. 120, p. 25–36 (doi: 10.1016/j.rse.2011.11.026).

Dunham, E.C., Fones, E.M., Fang, Y., Lindsay, M.R., Steuer, C., Fox, N., Willis, M., Walsh, A., Colman, D.R., Baxter, B.K., Lageson, D., Mogk, D., Rupke, A., Xu, H., and others, 2020, An ecological perspective on dolomite formation in Great Salt Lake, Utah: Frontiers in Earth Science, v. 8, p. 24 (doi: 10.3389/feart.2020.00024).

Foga, S., Scaramuzza, P.L., Guo, S., Zhu, Z., Dilley, R.D., Beckmann, T., Schmidt, G.L., Dwyer, J.L., Joseph Hughes, M., and Laue, B., 2017, Cloud detection algorithm comparison and validation for operational Landsat data products: Remote Sensing of Environment, v. 194, p. 379–390 (doi: 10.1016/j.rse.2017.03.026).

Gandhi, G.M., Parthiban, S., Thummalu, N., and Christy, A., 2015, Ndvi: Vegetation change detection using remote sensing and gis – a case study of Vellore District: Procedia Computer Science, v. 57, p. 1199–1210 (doi: 10.1016/j.procs.2015.07.415).

Gitelson, A.A., Gritz, Y., and Merzlyak, M.N., 2003, Relationships between leaf chlorophyll content and spectral reflectance and algorithms for non-destructive chlorophyll assessment in higher plant leaves: Journal of Plant Physiology, v. 160, no. 3, p. 271–282 (doi: 10.1078/0176-1617-00887).

Gwynn, J.W., 2007, Great Salt Lake brine chemistry databases and reports 1966-2006: Utah Geological Survey Open-File Report 485, 22p.

Hahnenberger, M., and Nicoll, K., 2012, Meteorological characteristics of dust storm events in the

eastern Great Basin of Utah, U.S.A.: Atmospheric Environment, v. 60, p. 601–612 (doi: 10.1016/j.atmosenv.2012.06.029).

Hahnenberger, M., and Nicoll, K., 2014, Geomorphic and land cover identification of dust sources in the eastern Great Basin of Utah, U.S.A.: Geomorphology, v. 204, p. 657–672 (doi: 10.1016/j.geomorph.2013.09.013).

Hall, D.K., O'Leary, D.S., DiGirolamo, N.E., Miller, W., and Kang, D.H., 2021, The role of declining snow cover in the desiccation of the Great Salt Lake, Utah, using MODIS data: Remote Sensing of Environment, v. 252, no. 4, p. 112106 (doi: 10.1016/j.rse.2020.112106).

Hansen, C.H., Dennison, P., Burian, S., Barber, M., and Williams, G., 2016, Hindcasting water quality in an optically complex system, *in* Proceedings of the 13th International Conference on Modelling, Monitoring and Management of Water Pollution (WP 2016), Venice, Italy, p. 35–44 (doi: 10.2495/WP160041).

Hardie, L.A., and Eugster, H.P., 1970, The evolution of closed-basin brines: Mineralogical Society of America Special Paper 3, p. 273–290.

Homewood, P., Mettraux, M., Vanden Berg, M., Foubert, A., Neumann, R., Newell, D., and Atwood, G., 2022, Onshore groundwater spring carbonate mounds to lacustrine microbialites, the perplexing record of a transitional Great Salt Lake carbonate shoreline at Lakeside, Utah: The Depositional Record, v. 8, no. 1, p. 9–38 (doi: 10.1002/dep2.148).

Huang, S., Tang, L., Hupy, J.P., Wang, Y., and Shao, G., 2021, A commentary review on the use of normalized difference vegetation index (NDVI) in the era of popular remote sensing: Journal of Forestry Research, v. 32, no. 1, p. 1–6 (doi: 10.1007/s11676-020-01155-1).

Hung, M.C., and Wu, Y.H., 2005, Mapping and visualizing the Great Salt Lake landscape dynamics using multi-temporal satellite images, 1972-1996: International Journal of Remote Sensing, v. 26, no. 9, p. 1815–1834 (doi: 10.1080/0143116042000298324).

Ingalls, M., Frantz, C.M., Snell, K.E., and Trower, E.J., 2020, Carbonate facies-specific stable isotope data record climate, hydrology, and microbial communities in Great Salt Lake, UT: Geobiology, v. 18, no. 5, p. 566–593 (doi: 10.1111/gbi.12386).

Jagniecki, E., Rupke, A., Kirby, S., and Inkenbrandt, P., 2021, Salt crust, brine, and marginal groundwater of Great Salt Lake's North Arm (2019 To 2021): Utah Geological Survey Report of Investigation 283, 40 p. (doi: 10.34191/RI-283).

Ji, L., Zhang, L., and Wylie, B., 2009, Analysis of dynamic thresholds for the normalized difference water index: Photogrammetric Engineering & Remote Sensing, no. 75, p. 1307–1317 (doi: 10.14358/PERS.75.11.1307).

Kokaly, R., Clark, R., Swayze, G., Livo, K.E., Hoefen, T., Pearson, N., Wise, R., Benzel, W., Lowers, H., Driscoll, R., and Klein, A., 2017, USGS Spectral Library Version 7: U.S. Geological Survey Data Series 1035, 61 p. (doi: 10.3133/ds1035).

Kulmatiski, A., Beard, K.H., Meyerson, L.A., Gibson, J.R., and Mock, K.E., 2011, Nonnative *Phragmites australis* invasion into Utah wetlands: Western North American Naturalist, v. 70, no. 4, p. 541-552 (doi: 10.3398/064.070.0414).

Lines, G.C., 1979, Hydrology and surface morphology of the Bonneville Salt Flats and Pilot Valley playa, Utah: U.S. Geological Survey Water-Supply Paper 2057, 107 p. (doi: 10.3133/wsp2057).

McFeeters, S.K., 1996, The use of the Normalized Difference Water Index (NDWI) in the delineation of open water features: International Journal of Remote Sensing, v. 17, no. 7, p. 1426–1432 (doi: 10.1080/01431169608948714).

Mohammed, I.N., and Tarboton, D.G., 2012, An examination of the sensitivity of the Great Salt Lake to changes in inputs: Water Resources Research, v. 48, no. 11, 17 p. (doi: 10.1029/2012WR011908).

Naftz, D., Angeroth, C., Freeman, M., Rowland, R., and Carling, G., 2013, Monitoring change in Great Salt Lake: Eos, Transactions American Geophysical Union, v. 94, no. 33, p. 289–290 (doi: 10.1002/2013EO330001).

Newell, D.L., Jensen, J.L., Frantz, C.M., and Vanden Berg, M.D., 2017, Great Salt Lake (Utah) microbialite $\delta^{13}C$, $\delta^{18}O$, and $\delta^{15}N$ record fluctuations in lake biogeochemistry since the Late Pleistocene: Geochemistry, Geophysics, Geosystems, v. 18, no. 10, p. 3631–3645 (doi: 10.1002/2017GC007078).

Nicoll, K., Hahnenberger, M., and Goldstein, H.L., 2020, 'Dust in the wind' from source-to-sink – analysis of the 14-15 April 2015 storm in Utah: Aeolian Research, v. 46, p. 100532 (doi: 10.1016/j.aeolia.2019.06.002).

Null, S.E., and Wurtsbaugh, W.A., 2020, Water development, consumptive water uses, and the Great Salt Lake *in* Baxter, B.K. and Butler, J.K., editors, Great Salt Lake biology: A terminal lake in a time of change: Cham, Switzerland, Springer, p. 1–21 (doi: https://doi.org/10.1007/978-3-030-40352-2).

Otsu, N., 1979, A threshold selection method from

gray-level histograms: IEEE Transactions on Systems, Man, and Cybernetics, v. 9, no. 1, p. 62–66.,

Pace, A., Bourillot, R., Bouton, A., Vennin, E., Galaup, S., Bundeleva, I., Patrier, P., Dupraz, C., Thomazo, C., Sansjofre, P., Yokoyama, Y., Franceschi, M., Anguy, Y., Pigot, L., Virgone, A, and Visscher, P.T., 2016, Microbial and diagenetic steps leading to the mineralisation of Great Salt Lake microbialites: Scientific Reports, v. 6, no. 1, p. 31495 (doi: 10.1038/srep31495).

Perry, K., Crosman, E.T., and Hoch, S., 2019, Results of the Great Salt Lake dust plume study (2016-2018): University of Utah, Department of Atmospheric Sciences, 305 p.

Radwin, M., and Bowen, B.B., 2021, Mapping mineralogy in evaporite basins through time using multispectral Landsat Data: examples from the Bonneville Basin, Utah, USA: Earth Surface Processes and Landforms., v. 46, no. 6, p. 1160-1176 (doi: 10.1002/esp.5089).

Reynolds, R.L., Yount, J.C., Reheis, M., Goldstein, H., Chavez, P., Fulton, R., Whitney, J., Fuller, C., and Forester, R.M., 2007, Dust emission from wet and dry playas in the Mojave Desert, USA: Earth Surface Processes and Landforms, v. 32, no. 12, p. 1811–1827 (doi: 10.1002/esp.1515).

Roney, H.C., Booth, G.M., and Cox, P.A., 2009, Competitive exclusion of cyanobacterial species in the Great Salt Lake: Extremophiles, v. 13, no. 2, p. 355–361 (doi: 10.1007/s00792-008-0223-1).

Rupke, A., and Boden, T., 2020, Great Salt Lake north arm salt crust monitoring, spring 2017 update: Utah Geological Survey Open-File Report 714, 13 p. (doi: 10.34191/OFR-714).

Rupke, A., Boden, T., and Nielsen, P., 2016, Great Salt Lake's north arm salt crust: Utah Geological Survey Report of Investigation 276, 40 p. (doi: 10.34191/RI-276).

Rupke, A., and McDonald, A., 2012, Great Salt Lake brine chemistry database, 1966-2011: Utah Geological Survey Open-File Report 596 (doi: 10.34191/OFR-596).

Skiles, S.M.K., Mallia, D.V., Hallar, A.G., Lin, J.C., Lambert, A., Petersen, R., and Clark, S., 2018, Implications of a shrinking Great Salt Lake for dust on snow deposition in the Wasatch Mountains, UT, as informed by a source to sink case study from the 13-14 April 2017 dust event: Environmental Research Letters, v. 13, no. 12 (doi: 10.1088/1748-9326/aaefd8).

Smith, B.P., Ingalls, M., Trower, E.J., Lingappa, U.F., Present, T.M., Magyar, J.S., and Fischer, W.W., 2020, Physical controls on carbonate intraclasts – modern flat pebbles from Great Salt Lake, Utah: Journal of Geophysical Research: Earth Surface, v. 125, no. 11 (doi: 10.1029/2020JF005733).

Tamiminia, H., Salehi, B., Mahdianpari, M., Quackenbush, L., Adeli, S., and Brisco, B., 2020, Google Earth Engine for geo-big data applications – a meta-analysis and systematic review: ISPRS Journal of Photogrammetry and Remote Sensing, v. 164, p. 152–170 (doi: 10.1016/j.isprsjprs.2020.04.001).

Tiede, D., Sudmanns, M., Augustin, H., and Baraldi, A., 2021, Investigating ESA Sentinel-2 products' systematic cloud cover overestimation in very high altitude areas: Remote Sensing of Environment, v. 252, p. 112163 (doi: 10.1016/j.rse.2020.112163).

Wang, S.-Y., Gillies, R.R., and Reichler, T., 2012, Multidecadal drought cycles in the Great Basin recorded by the Great Salt Lake – modulation from a transition-phase teleconnection: Journal of Climate, v. 25, no. 5, p. 1711–1721 (doi: 10.1175/2011JCLI4225.1).

Weimer, B.C., Rompato, G., Parnell, J., Gann, R., Ganesan, B., Navas, C., Gonzalez, M., Clavel, M., and Albee-Scott, S., 2009, Microbial biodiversity of Great Salt Lake, Utah: Natural Resources and Environmental Issues, v. 15, Article 3.

Wine, M.L., Null, S.E., DeRose, R.J., and Wurtsbaugh, W.A., 2019, Climatization—negligent attribution of Great Salt Lake desiccation – a comment on Meng (2019): Climate, v. 7, no. 5, p. 67 (doi: 10.3390/cli7050067).

Wu, Q., 2020, geemap: A Python package for interactive mapping with Google Earth Engine: Journal of Open Source Software, v. 5, no. 51, p. 2305 (doi: 10.21105/joss.02305).

Wurtsbaugh, W.A., Miller, C., Null, S.E., DeRose, R.J., Wilcock, P., Hahnenberger, M., Howe, F., and Moore, J., 2017, Decline of the world's saline lakes: Nature Geoscience, v. 10, no. 11, p. 816–821 (doi: 10.1038/ngeo3052).

Wurtsbaugh, W., Miller, C., Null, S., Wilcock, P., Hahnenberger, M., and Howe, F., 2016, Impacts of water development on Great Salt Lake an d the Wasatch Front: Utah State University, Watershed Sciences Faculty Publications, Paper 875, 9 p.

Wurtsbaugh, W.A., and Sima, S., 2022, Contrasting Management and Fates of Two Sister Lakes – Great Salt Lake (USA) and Lake Urmia (Iran): Water, v. 14, no. 19, p. 23 (doi: https://doi.org/10.3390/w14193005).